Communications on Applied Mathematics and Computation
https://doi.org/10.1007/s42967-024-00443-5

ORIGINAL PAPER

A Three-Dimensional Tumor Growth Model and Its Boundary Instability

Jian-Guo Liu[1] · Thomas Witelski[1] · Xiaoqian Xu[2] · Jiaqi Zhang[2]

Received: 27 December 2023 / Revised: 27 May 2024 / Accepted: 28 June 2024

Abstract
In this paper, we investigate the instability of growing tumors by employing both analytical and numerical techniques to validate previous results and extend the analytical findings presented in a prior study by Feng et al. (Z Angew Math Phys 74:107, 2023). Building upon the insights derived from the analytical reconstruction of key results in the aforementioned work in one dimension and two dimensions, we extend our analysis to three dimensions. Specifically, we focus on the determination of boundary instability using perturbation and asymptotic analysis along with spherical harmonics. Additionally, we have validated our analytical results in a two-dimensional (2D) framework by implementing the Alternating Direction Implicit (ADI) method. Our primary focus has been on ensuring that the numerical simulation of the propagation speed aligns accurately with the analytical findings. Furthermore, we have matched the simulated boundary stability with the analytical predictions derived from the evolution function, which will be defined in subsequent sections of our paper. This alignment is essential for accurately determining the stability or instability of tumor boundaries.

Keywords Tumor growth · Boundary instability · Asymptotic analysis · Spherical harmonics · Bessel functions

Mathematics Subject Classification Primary: 35R35 · 70K50 · 74G10; Secondary: 92C10

✉ Jiaqi Zhang
jz374@duke.edu

Jian-Guo Liu
jian-guo.liu@duke.edu

Thomas Witelski
witelski@math.duke.edu

Xiaoqian Xu
xiaoqian.xu@dukekunshan.edu.cn

[1] Mathematics Department, Duke University, Durham, NC, USA

[2] Zu Chongzhi Center for Mathematics and Computational Sciences, Duke Kunshan University, Kunshan 215316, Jiangsu, China

Published online: 26 December 2024

1 Introduction

Cancer is one of the major concerning diseases around the world, and the mathematical study of tumor growth has proved to be meaningful in providing insights for treatments. Therefore, investigating partial differential equation (PDE) models in the context of tumor growth is of great importance [7, 11, 12].

Recent advancements in tumor growth modeling have emphasized nonlinear dynamics, boundary behaviors, and stability under perturbations. Cristini et al. (2003) identified key dimensionless parameters controlling tumor evolution in [7], delineating growth models influenced by vascularization. Greenspan (1972) provided a foundational diffusion-based free boundary model for solid tumor growth in [12], while Friedman and Reitich (2000) revealed numerous asymmetric solutions in stationary tumor models in [11]. These highlight the interaction between mathematical parameters and tumor morphology. Moreover, Feng et al. (2023) examined the tumor boundary stability in [10], finding that tumor boundaries in vitro remain stable under various conditions, while in vivo boundaries exhibit the instability when the nutrient consumption rate exceeds certain thresholds, influenced by the wave numbers of domain perturbations. Improved numerical schemes for tumor growth PDE models include the novel prediction-correction reformulation that accurately approximates the front propagation of speed with the strong nonlinearity introduced by Liu et al. (2018) in [21]. These studies underline the complex interplay between biological and mathematical factors in tumor growth, guiding our research on the stability of tumor growth models after perturbation in three dimensions. One may notice that there are extensive studies regarding the real datum for the tumor growth in the two-dimensional (2D) space, such as [8, 14, 15]. However, we would like to remark that 2D models are still simplifications of real three-dimensional (3D) tumor models, see [3, 4] for more discussions.

The main question that we are focusing on is the instability of the tumor boundary induced by nutrient consumption and supply, which is significant since previous research has suggested the shape of tumors as one of the crucial criteria to determine whether a tumor is benign or malignant [1, 5, 23, 25]. Specifically, we investigate this based on [10], using finite difference numerical schemes to match up to the 2D analytical results presented in [10], as well as extending the results to a 3D perturbed spherical scenario. We first apply the Alternating Direction Implicit (ADI) numerical scheme, as in Witelski (2003), to validate against the 2D analytical results in Feng (2023) on tumor dynamics. Following this, we introduce spherical harmonics as a perturbation method, expanding our tumor model to a 3D framework. In this extension, we employ modified Bessel functions, hyperbolic trigonometric functions, and asymptotic expansions to derive analytical results for the 3D scenario. This study is significant from different perspectives. Firstly, the findings reported in [10] are predominantly based on analytical techniques, and the introduction of numerical simulations offers an alternative perspective on the 2D tumor PDE model, shedding light on the boundary instability. Moreover, the extension of our investigation into 3D tumor dynamics, both analytically and numerically, has practical implications, providing deeper insights into the malignant potential of tumors.

In this paper, we begin by describing the model, detailing both in vitro and in vivo nutrient models. We then focus on 2D numerical schemes, matching our numerical simulations to the results in [10]. Subsequently, we investigate the boundary stability and introduce our analytical approach for constructing 3D scenarios, highlighting the distinction between our 2D and 3D tumor boundary instability. The paper concludes with a summary of our findings and a discussion of future research directions.

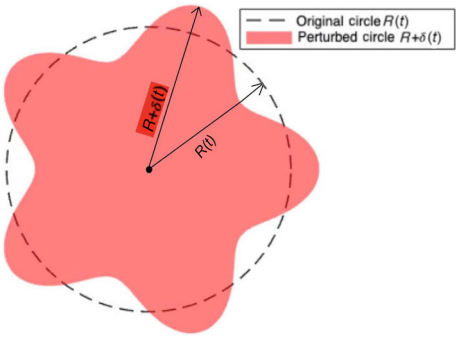

Fig. 1 Schematic figure of the tumor and the surrounding exterior. The cell population density ρ is defined in the red shaded tumoral region; $c^{(o)}$ and $c^{(i)}$ are the nutrient concentration defined outside and inside the red shaded tumoral region [10]

2 Model Formulation

The full PDE model in [10] that we are focusing on is based on the sharp interface limit of a cell density model. In Fig. 1, we present a schematic representation of the tumor geometry. This depiction illustrates a 2D circular domain with the radius R, encapsulated within a nutrient exterior. This simplified representation serves as a conceptual aid; the actual geometry of the tumor, governed by the equations detailed subsequently, can be any general domain. Our focus on basic geometric forms, such as the axisymmetric circle in two dimensions or the sphere in three dimensions (as explored in Sect. 5), is instrumental. This focus allows us to distill the essential physics of the model. By employing these simplified shapes, specifically the spherically symmetric sphere in our 3D analysis, we aim to elucidate the fundamental principles underlying the behavior of the model.

2.1 Finite-*k* Compressible Model

Following this, we are interested in physical properties such as the tumor density, the nutrient concentration, and the pressure. Specifically, we denote $\rho(x,t)$ as the cell population density, and $c(x,t)$ as the nutrient concentration. The production rate of tumor cells, G_0, depends only on the nutrient concentration, where we use $G(c) = G_0 c$ as a growth function in this paper for simplicity. To represent the tumoral region at time t, we denote the support of ρ as $D = \{x|\rho > 0\}$. Here, we assume the tumoral region expands with a finite speed governed by Darcy's law $v = -\nabla p|_{\partial\Omega}$ via the pressure $p(\rho) = \rho^k$ [10]. In these models, we use Darcy's law because the flow within the tumor or biological tissue can be highly nonlinear, meaning that small changes in density can lead to large changes in flow or vice versa. A power law is a simple way to capture such nonlinear effects. The positive power $k > 0$ ensures the consistency with physical laws, since the pressure in a fluid or gas typically increases as the density increases. Additionally, a positive power k in the equation ensures that the pressure $p(\rho)$ is a well-defined, real-valued function for all positive values of the density ρ. Furthermore, $k > 0$ in the pressure $p(\rho) = \rho^k$ ensures that the support of ρ is compact. Thus, the density ρ is governed by a Porous Medium Equation (PME) type equation:

$$\frac{\partial \rho}{\partial t} - \nabla \cdot (\rho \nabla p(\rho)) = G_0 \rho c, \quad x \in \mathbb{R}^n, \quad t \geqslant 0, \tag{1}$$

where $n = 2$ or $n = 3$.

The consumption, exchange, and diffusion of the nutrient are governed by the following reaction-diffusion equation for the nutrient concentration c:

$$\tau \frac{\partial c}{\partial t} - \nabla^2 c + \Psi(\rho, c) = 0, \tag{2}$$

where $\tau \ll 1$ is the characteristic time scale of nutrient evolution, and $\Psi(u, c)$ describes the overall effects of the nutrient supply regime outside the tumor and the nutrient consumption by cells inside the tumor [10].

Specifically, the overall function $\Psi(\rho, c)$ is mathematically written as $\Psi(\rho, c) = \lambda \rho c \cdot \mathbb{1}_D - \tilde{\lambda}(c_B - c) \cdot \mathbb{1}_{D^c}$. For simplicity, we set $\tilde{\lambda} = 1$ and $\lambda > 0$. $\mathbb{1}_D$ indicates the indicator function of the set D (the region of the tumor), and $\mathbb{1}_{D^c}$ is the indicator function of the complement of the set D [10], and we also use $\partial D(t)$ to denote the evolving tumor boundary. The indicator function of a set A is defined such that it assigns a value of 1 to an element x if x is in the set A, and a value of 0 if x is not in the set A.

For simplicity in the later analysis, we consider the following elliptic formulation by dropping the time derivative, which is reasonable since $\tau \ll 1$:

$$-\nabla^2 c + \Psi(\rho, c) = 0. \tag{3}$$

This further yields

$$-\nabla^2 c + \lambda \rho c = 0 \ \text{ for } \ x \in D(t), \tag{4}$$

where $n = 2, 3$, $D(t)$ is the tumor region, and λ is the consumption rate [10].

Positivity of density in our model is crucial both theoretically and computationally. According to the maximum principle, the density ρ is always non-negative. In scenarios where the power of the PME, denoted by k, equals 1, the instantaneous positivity of ρ is guaranteed. However, for $k > 1$, it is well-known that the density ρ can approach zero and ρ has only C^α regularity, as detailed in [27]. Active research focuses on developing numerical schemes that preserve the positivity, including flux splitting type schemes applicable to both second-order and fourth-order degenerate parabolic equations [2, 13, 22].

Additionally, the positivity can also be derived using the method detailed in [24]. Specifically, in our model, (1) can be reformulated as a transport-reaction equation:

$$\partial_t \rho + \nabla \cdot (\rho v) = G_0 \rho, \quad v = -\frac{k}{k-1} \nabla \rho^{k-1}.$$

In the context of this variational problem, we take variation with respect to the flow map X^ϵ, where $X^\epsilon = v(X^\epsilon, t)$ and $X^\epsilon(x, 0) = x$, This provides an alternative method to preserve the positivity of the density. Furthermore, preserving the positivity is significant for related fourth-order degenerate equations. Unlike the maximum principle, the positivity here stems from the specific choice of free energy. This concept is employed in the Flory-Huggins style Cahn-Hilliard equation with a logarithmic potential to ensure the positivity [6].

The illustrations of the behavior in the model in the form of the two PDEs in (1) and (2) are shown in Figs. 2 and 3. These figures showcase simulations performed with the ADI method, an effective numerical technique for solving 2D parabolic PDEs, such as the PME and classic diffusion equations. This method discretizes spatial derivatives in alternating directions across subsequent time steps, thereby reducing the computational complexity by decoupling the resulting tridiagonal systems [28]. Specifically, the ADI method alternates between treating diffusion implicitly in one spatial direction and explicitly in the other within each time step. This approach not only simplifies the computational steps but also achieves second-order accuracy over the complete time step due to the symmetric nature of the discretization.

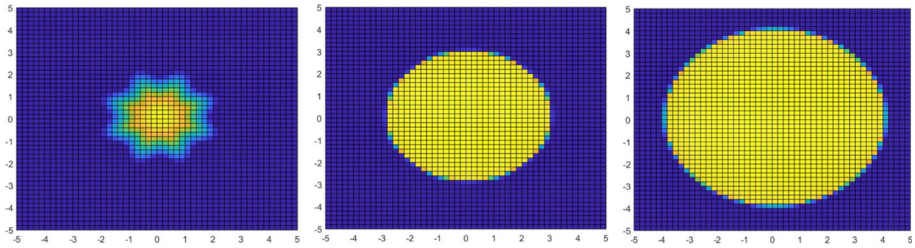

Fig. 2 The 2D tumor growth boundary evolution with $\lambda = 0.5$ (three time profiles evolving from left to right) for an initial perturbation with the wave number $m = 8$

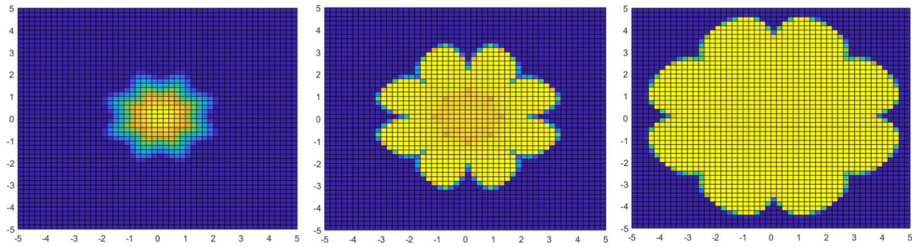

Fig. 3 The 2D tumor growth boundary evolution with $\lambda = 40$ (three time profiles evolving from left to right) for an initial perturbation with the wave number $m = 8$

However, the implementation of the ADI scheme, while straightforward, exhibited a weakly decoupled system that lacked the stability for varied parameter inputs. To address this challenge, we explored multiple splitting approaches within the ADI method. Specifically, we experimented with various sets of splittings, such as 1/2 and 1/2, 1/3 and 2/3, 1/4 and 3/4, and so forth. Among all the tested sets, we identified that the 1/8 and 7/8 splitting provided the most stable system. The stability of the ADI scheme was assessed by observing whether different parameter values consistently produced the same simulation results for the tumor boundary shape. This consistency indicated the stability of the splitting approach in our ADI scheme, ensuring reliable performance across varied parameter inputs. Therefore, we will use this splitting in our model to numerically simulate tumor growth, where the details are demonstrated in Appendixes A.1.1 and A.2.1.

2.2 Incompressible $k = \infty$ Model

Taking the incompressible limit of $k \to \infty$, and considering the patch solutions $\rho_\infty = \mathbb{1}_{D_\infty}$, $D_\infty \subset \mathbb{R}^n$, yield the simplified versions of (1) and (3):

$$\begin{cases} -\nabla^2 p_\infty = G_0 c \ \text{ for } \ x \in D_\infty(t), \\ p_\infty = 0 \ \text{ for } \ x \in \mathbb{R}^n \backslash D_\infty(t). \end{cases} \tag{5}$$

The boundary conditions (BCs) for the pressure p in the in vitro model are that the pressure is bounded everywhere and the pressure value and its derivative are zero at the boundary. Therefore, these give us the complete PDE problem for solving the pressure p for the in vitro model

$$-\nabla^2 c + \lambda c = 0 \ \text{ for } \ x \in D_\infty(t), \tag{6}$$

where $n = 2, 3$, and the in vitro and in vivo models will be introduced shortly in Sect. 2.2 [10].

From now on, all pressures are $p = p_\infty$, and we omit the subscript. Therefore, combining (5) and (6), we can denote

$$u = p + \frac{G_0}{\lambda} c \qquad \text{satisfying} \quad \nabla^2 \left(p + \frac{G_0}{\lambda} c \right) = 0. \tag{7}$$

This gives us the Laplace's equation for u, which will be useful for later constructions.

The domain we are considering here is a disk or sphere with the radius R, where the solution is bounded everywhere. The boundary and initial conditions (ICs) for the above PDEs will be introduced for the simplified versions of this full model in the following subsections. Furthermore, the boundary moving speed in the direction normal to the boundary at a point x, denoted by $\sigma(x)$, is given by

$$\sigma(x) = -\nabla p_\infty \cdot \hat{n}(x), \tag{8}$$

where $\hat{n}(x)$ is the outer unit normal vector at $x \in \partial D_\infty(t)$. This gives us the general axisymmetric interface motion equation

$$\frac{\mathrm{d}R}{\mathrm{d}t} = -\partial_r p(R(t)). \tag{9}$$

Our density model can be considered as a phase field approximation of the sharp interface model; for a rigorous treatment of the sharp interface limit/ incompressible limit, see Feng et al. (2024) [9]. Interestingly, identifying an alternative phase field model that is more computationally and analytically tractable could significantly advance the study of this critical problem in cancer treatment, as discussed by Baskaran et al. (2013) [2].

2.3 Two Models for the Nutrient Distribution

Following the general PDE model in (3) and (6), we consider the two simplified versions with different concentration assumptions, as introduced in [10], which are the in vitro and in vivo models. We study the boundary stability of the radially symmetric scenario under these two nutrient models, where R is the radius of the tumor before perturbation.

2.3.1 The in Vitro Model

For the in vitro version, it is assumed that the tumor is surrounded by a liquid and the exchange rate with the background is extremely high so that c matches c_B on the tumor boundary [10]. This gives us a constant nutrient concentration outside the tumor and quasi-steady inside the tumor. The in vitro concentration assumption outside the tumoral region coupled with (6) gives us the system of equations for the in vitro regime [10]:

$$\begin{cases} -\nabla^2 c + \lambda c = 0 \ \text{ for } \ x \in D_\infty(t), \\ c = c_B \ \text{ for } \ x \in \mathbb{R}^n \backslash D_\infty(t), \end{cases} \tag{10}$$

where $n = 2, 3$ and $\lambda > 0$ is the consumption rate. Therefore, (10) together with the BC $c(\partial D) = c_B$ gives us the complete PDE problem for solving the concentration c for the in vitro regime model. We only need to solve for the concentration c inside the tumor since c is always constant outside the tumor.

2.3.2 The in Vivo Model

For the in vivo version, the nutrient is transported by vessels outside the tumor and reaches c_B at the far field. Correspondingly, it is assumed that the exchange rate outside the tumor is determined by the concentration difference from the background, i.e., $c_B - c$ [10]. The in vivo concentration assumption outside the tumoral region coupled with (6) gives us the system of equations for the in vivo regime [10]:

$$\begin{cases} -\nabla^2 c + \lambda c = 0 \ \text{ for } \ x \in D_\infty(t), \\ -\nabla^2 c = c_B - c \ \text{ for } \ x \in \mathbb{R}^n \backslash D_\infty(t), \end{cases} \tag{11}$$

where $n = 2, 3$, and the concentration is quasi-steady inside and outside the tumor. We assume the tumor is axisymmetric, and we denote the concentration inside the tumor as $c^{(i)}(r, t)$, and the concentration outside the tumor as $c^{(o)}(r, t)$. The solution for concentration is everywhere bounded, and BCs for concentration c in the in vitro model are

$$\begin{cases} c^{(i)}(R, t) = c^{(o)}(R, t), \\ \dfrac{\partial c^{(i)}(r, t)}{\partial r}\Big|_{r=R} = \dfrac{\partial c^{(o)}(r, t)}{\partial r}\Big|_{r=R}. \end{cases} \tag{12}$$

Therefore, (11) and (12) give us the complete PDE problem for solving the concentration c for the in vivo regime model.

The PDE problem for the pressure p in the in vivo model is identical to that in the in vitro model. Therefore, (5) along with the BCs outlined before Sect. 2.1, comprehensively defines the PDE problem for determining the pressure p in both the in vitro and in vivo models.

3 The 2D Problem

In this section, we examine the 2D analytical findings on the tumor boundary stability and instability as presented in [10], focusing on the radially symmetric boundary. In two dimensions, the tumoral region is considered a disk with the radius R for simplicity. This aims to establish the foundational equations pertinent to our research and facilitate a comparative analysis with the 3D results we obtained. Specifically, in Sect. 3.1, we skip their calculation details and provide a comprehensive overview of their procedural steps. Subsequently, in Sect. 3.2, we state their results for two dimensions.

3.1 Overview of the Steps

In both the in vitro and in vivo models, similar methodologies are employed, yet they yield distinct results. In this section, we primarily focus on the more complex in vivo scenario as an illustrative example. The results for both the in vitro and in vivo models are presented in Sect. 3.2.

Step 1: Solve radial symmetric solution

In [10], the authors solve the nutrient concentration using the modified Bessel functions of the second kind $I_n(r)$ and $K_n(r)$. Then, they solve the pressure p_∞ and use the symmetry to derive $p_\infty(r, t)$. Following (9), the velocity of the boundary for the in vitro model is

$$\frac{\mathrm{d}R}{\mathrm{d}t} = \frac{G_0 c_B I_1(\sqrt{\lambda}R)}{\sqrt{\lambda} I_0(\sqrt{\lambda}R)} \tag{13}$$

and for the in vivo model:

$$\frac{\mathrm{d}R}{\mathrm{d}t} = \frac{G_0 c_B K_1(R) I_1(\sqrt{\lambda}R)}{\lambda K_0(R) I_1(\sqrt{\lambda}R) + \sqrt{\lambda} K_1(R) I_0(\sqrt{\lambda}R)}. \tag{14}$$

Step 2: Define the perturbation in terms of the perimeter curve

If we denote $B = \partial D$, then $\tilde{B}$ is the tumor boundary after perturbation. At time t, the authors introduce a perturbation characterized by an amplitude $\delta(t)$ and the boundary of this perturbation is described as follows:

$$\begin{cases} B_\delta(\phi) = \{(r, \phi) | r = R(t), \phi \in [-\pi, \pi)\}, \\ \tilde{B}_\delta(\phi) = \{(r, \phi) | r = R(t) + \delta(t)\cos(m\phi), \phi \in [-\pi, \pi)\}. \end{cases} \tag{15}$$

Step 3: Expression of asymptotic solutions on the perturbed region

The perturbed solutions $\tilde{c}$ and $\tilde{p}$ have the following asymptotic expansions:

$$\begin{cases} \tilde{c}(r, \phi, t) = c_0(r, t) + \delta(t)\tilde{c}_1(r, \phi, t) + O(\delta^2), \\ \tilde{p}(r, \phi, t) = p_0(r, t) + \delta(t)\tilde{p}_1(r, \phi, t) + O(\delta^2), \end{cases} \tag{16}$$

where the leading order terms c_0 and p_0 correspond to the unperturbed solutions solved in Step 1. The main response corresponding to the perturbation is captured by the first-order terms $c_1(r, \phi, t)$ and $p_1(r, \phi, t)$. The higher-order terms are represented by $O(\delta^2)$. Here, for the linear problem involving c_1 and p_1, we can solve for a single m-mode from the Fourier series independently. For further details, please refer to Sect. 5.2 in [10]. This allows us to simplify the expansions and approximate them as

$$\begin{cases} \tilde{c}_1(r, \phi, t) \approx c_1(r, t)\cos(m\phi), \\ \tilde{p}_1(r, \phi, t) \approx p_1(r, t)\cos(m\phi). \end{cases} \tag{17}$$

Step 4: Equations for the first order terms

Plug the asymptotic solutions into the model on $\tilde{D}(t)$ and solve for $c_1^{(i)}$ and $c_1^{(o)}$:

$$\begin{cases} -\nabla^2 c_1^{(i)}(r, \phi, t) + \lambda c_1^{(i)}(r, \phi, t) = 0, \\ -\nabla^2 c_1^{(o)}(r, \phi, t) + c_1^{(o)}(r, \phi, t) = 0. \end{cases} \tag{18}$$

Thus,

$$\begin{cases} c_1^{(i)}(r, t) = c_B a_1(t) I_m(\sqrt{\lambda}r) \quad \text{for } r \leqslant R(t), \\ c_1^{(o)}(r, t) = c_B b_1(t) K_m(r) \quad \text{for } r \geqslant R(t), \end{cases} \tag{19}$$

where m represents the harmonic order of the coefficients in the Fourier series expansion. Remember that we denote the concentration inside the tumor as $c^{(i)}(r, t)$, and the concentration outside the tumor as $c^{(o)}(r, t)$ [10]. On the other hand, p_1 solves

$$\nabla^2 p_1(r, \phi, t) = G_0 c_1^{(i)}(r, \phi, t) \text{ in } \tilde{D}(t). \tag{20}$$

Step 5: Determine the coefficients by matching the boundary

The authors evaluate the perturbed solution on the boundary point $\tilde{B}(R+\delta\cos(m\phi),\phi)$ by first taking the Taylor expansion around R with respect to the first variable up to first order:

$$\begin{aligned} c^{(i)}(R+\delta\cos(m\phi),\phi) &= c^{(o)}(R+\delta\cos(m\phi),\phi) \\ &= c_0(R)+\delta\partial_r c_0(R)\cos(m\phi)+\delta c_1(R)\cos(m\phi),\ \forall\phi\in[-\pi,\pi], \end{aligned}$$

$$\begin{aligned} \partial_r c^{(i)}(R+\delta\cos(m\phi),\phi) &= \partial_r c^{(o)}(R+\delta\cos(m\phi),\phi) \\ &= \partial_r c_0(R)+\partial_r^2 c_0(R)\delta\cos(m\phi)+\delta\partial_r c_1(R)\cos(m\phi),\ \forall\phi\in[-\pi,\pi]. \end{aligned} \tag{21}$$

Then by using the BCs for c_1, we require the solution to be bounded everywhere and $c(\infty,\phi)=c_B$ for any $\phi\in[-\pi,\pi)$ yields

$$c_1^{(o)}(\infty,t)=0. \tag{22}$$

Using the above BCs, the coefficients $a_1(R(t))$ and $b_1(R(t))$ in (19), are determined.

Step 6: Determine p_1 for the amplitude evolution equation $\delta^{-1}\frac{\mathrm{d}\delta}{\mathrm{d}t}$

The perturbed pressure solution p satisfies the BCs $p=0$ at $\tilde{B}_\delta$. Evaluating p at $\tilde{B}(R+\delta\cos(m\phi))\in\tilde{B}_\delta$, which yields the leading order equation for $\delta\to 0$

$$p(R+\delta\cos(m\phi),\phi)=p_0(R)+\partial_r p_0(R)\delta\cos(m\phi)+p_1(R)\delta\cos(m\phi), \tag{23}$$

where $O(1)$ yields $\frac{\mathrm{d}R}{\mathrm{d}t}=-\partial_r p_0(R)$, and $O(\delta)$ yields the linear $\frac{\mathrm{d}\delta}{\mathrm{d}t}$ equation. Since $p(R+\delta\cos(m\phi),\phi)=p_0(R)=0$,

$$\partial_r p_0(R)+p_1(R)=0. \tag{24}$$

By using the expressions of c_1 and p_0, the particular solution of p_1 can be determined. After this, plugging the expression of p into the normal boundary speed (Darcy's law) and taking the Taylor expansion for the r variable yield the leading order equation for $\delta\to 0$

$$\frac{\mathrm{d}R}{\mathrm{d}t}+\frac{\mathrm{d}\delta}{\mathrm{d}t}\cos(m\phi)=-(\partial_r p_0(R)+\partial_r^2 p_0(R)\delta\cos(m\phi)+\partial_r p_1(R)\delta\cos(m\phi)), \tag{25}$$

which simplifies to

$$\delta^{-1}\frac{\mathrm{d}\delta}{\mathrm{d}t}=-(\partial_r^2 p_0(R)+\partial_r p_1(R))+O(\delta). \tag{26}$$

This is used to determine the evolution of the perturbation magnitude by the sign of $\delta^{-1}\frac{\mathrm{d}\delta}{\mathrm{d}t}$. Specifically, if it is positive, then it implies the growth of the magnitude, which leads to the instability with the growing perturbation. If it is negative, then it implies the decay of the perturbation amplitude and leads to the stability of the tumor boundary.

3.2 Results of 2D Tumor Boundary Stability/Instability in [10]

In conclusion, given $G_0>0$, $c_B>0$, $\lambda>0$, and $m\in\mathbb{N}^+$. When the radius of the tumor is around R. For the in vitro model, $\delta^{-1}\frac{\mathrm{d}\delta}{\mathrm{d}t}$ is given by

$$\delta^{-1}\frac{\mathrm{d}\delta}{\mathrm{d}t}=\frac{G_0 c_B I_1(\sqrt{\lambda}R)}{I_0(\sqrt{\lambda}R)}\left(\frac{I_1'(\sqrt{\lambda}R)}{I_1(\sqrt{\lambda}R)}-\frac{I_m'(\sqrt{\lambda}R)}{I_m(\sqrt{\lambda}R)}\right)\overset{\text{def}}{=}F_3(\lambda,m,R). \tag{27}$$

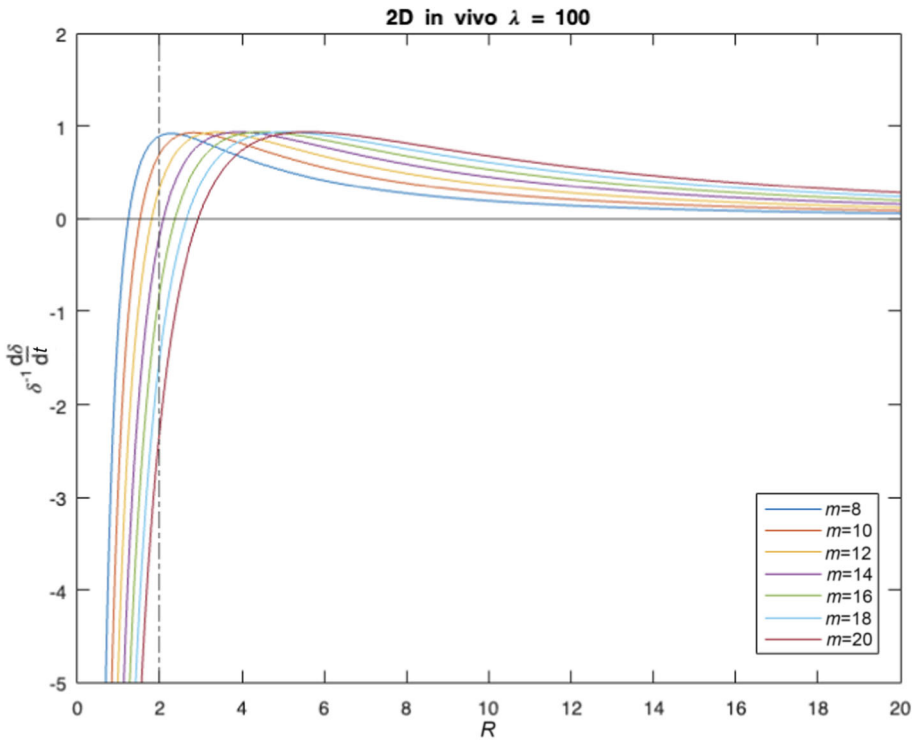

Fig. 4 2D in vivo evolution function with $G_0 = 1$, $c_B = 100$; $\lambda = 100$ and $R \in [0, 20]$

For the **in vivo** model, $\delta^{-1}\frac{d\delta}{dt}$ is given by

$$\begin{aligned}\delta^{-1}\frac{d\delta}{dt} &= \frac{G_0 c_B m}{\sqrt{\lambda}RC(R)}\left(\frac{C_1(R)}{C_m(R)}K_m(R)I_m(\sqrt{\lambda}R) - K_1(R)I_1(\sqrt{\lambda}R)\right)\\ &\quad - \frac{G_0 c_B}{C(R)}\left(\frac{C_1(R)}{C_m(R)}K_m(R)I_m'(\sqrt{\lambda}R) - K_1(R)I_1'(\sqrt{\lambda}R)\right)\\ &\stackrel{\text{def}}{=} F_4(\lambda, m, R),\end{aligned} \tag{28}$$

where $C(R) = \sqrt{\lambda}K_0(R)I_1(\sqrt{\lambda}R) + K_1(R)I_0(\sqrt{\lambda}R)$, and $C_j(R) = K_j'(R)I_j(\sqrt{\lambda}R) - \sqrt{\lambda}I_j'(\sqrt{\lambda}R)K_j(R)$. Here m denotes the wave number, and $I_n(x)$ and $K_n(x)$ are the modified Bessel functions of order n.

Therefore, the sign of the leading order terms of $\delta^{-1}\frac{d\delta}{dt}$ (such as $F_3(\lambda, m, R)$ and $F_4(\lambda, m, R)$ as shown above) determines the sign of $\delta^{-1}\frac{d\delta}{dt}$, thus implies the stability/instability of the tumor boundary after perturbation. The plots of the evolution function for the in vivo regime are shown in Figs. 4, 5. The simulations of the tumor boundary evolution using the ADI method are shown in Figs. 2, 3, where the detailed descriptions for the numerical scheme will be presented in Appendix A.

Remark 1 In the in vitro regime, both graphical and analytical analyses indicate that the growth of the perturbation amplitude and boundary stability are maintained. This holds

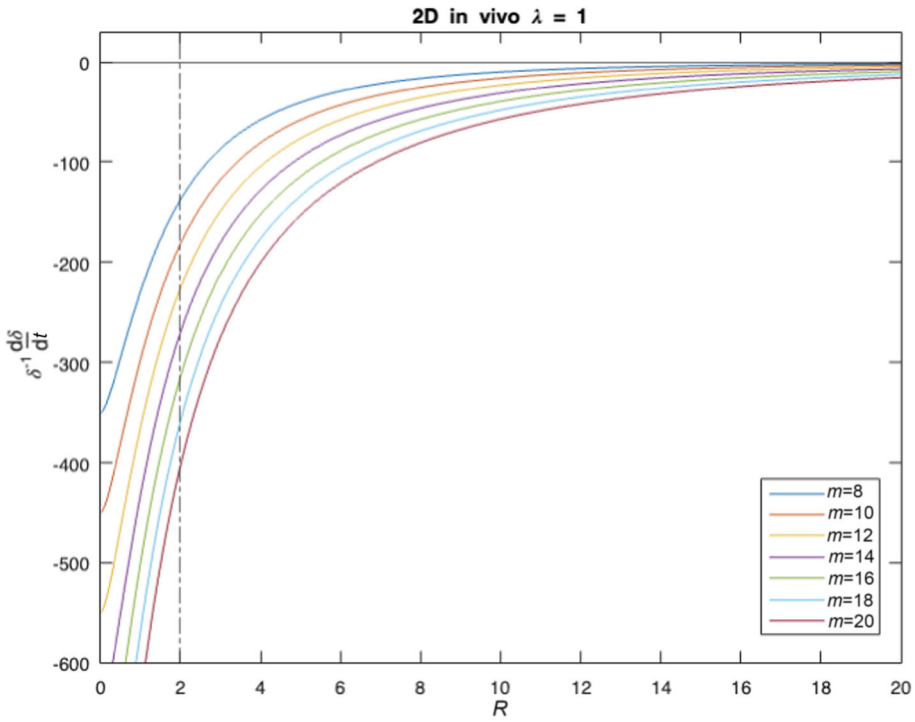

Fig. 5 2D in vivo evolution function with $G_0 = 1$, $c_B = 100$; $\lambda = 1$ and $R \in [0, 20]$

regardless of variables such as the consumption rate λ, the perturbation wave number $m \in \mathbb{N}$, and the tumor size R.

Remark 2 For the in vivo regime, we have the following.

i. When $0 < \lambda \leqslant 1$ (λ: nutrient consumption rate), the boundaries show the same qualitative behavior as the in vitro model.
ii. When $\lambda > 1$, for any fixed wave number $m \geqslant 2$, there exists a threshold $R^*(m)$ such that $F_4(\lambda, m, R) < 0$ for $0 < R < R^*(m)$, and $F_4(\lambda, m, R) > 0$ for $R > R^*(m)$. This is proved by checking the asymptotes of F_4. Also, fix a proper value of R_0, there exists m_0 such that $F_4(\lambda, m, R_0) > 0$ for $m < m_0$ and $F_4(\lambda, m, R_0) < 0$ for $m > m_0$. Lastly, as the tumor size expands, $R(t)$ exceeds more thresholds $R^*(m)$, therefore the corresponding wave number perturbation becomes unstable successively.

4 The 3D Problem

While the foundational configurations and methodologies in the 3D analysis are similar to those employed in the 2D case, the extension to a 3D framework in exploring the tumor growth model is of substantive significance. Primarily, this 3D approach yields results with higher applicability to real-world scenarios, enhancing the model's practical relevance. Additionally, the 3D model employs more intricate techniques, such as spherical harmonics, to capture the complexities of tumor growth. These advanced methodologies facilitate a deeper

understanding of the tumor boundary instability, a pivotal aspect of our study. The technical intricacies and the evolution function construction that elucidate the instability of the tumor boundary are detailed in Sects. 4.3 and 4.4.

In this section, we focus on analyzing the tumor growth model in a 3D scenario, examining it under both in vitro and in vivo nutrient conditions. Specifically, we explore the spherically symmetric model in a 3D context for these nutrient models before any perturbation, as detailed in Sects. 4.1 (in vitro) and 4.2 (in vivo). We then shift our attention to the stability of the 3D spherically symmetric model under these models, discussed in Sects. 4.3 (in vitro) and 4.4 (in vivo). A key part of our investigation involves reconstructing critical variables: the concentration (c), the pressure (p), and the boundary speed (σ) and analyzing their behaviors both before and after perturbations. We also derive the evolution function $\delta^{-1}\frac{\mathrm{d}\delta}{\mathrm{d}t}$ and use it to assess the stability of the tumor boundary, based on its sign. The critical threshold for the transition between the stability and instability is identified through the asymptotic analysis of spherical modified Bessel functions and hyperbolic functions, which play a significant role in the evolution function. Detailed results and methodologies are included in each respective section. In Sect. 5.1, we emphasize a comparative analysis between the in vitro and in vivo results, highlighting biological insights gained from this comparison.

4.1 3D Spherically Symmetric Solution for the in Vitro Model

For the 3D scenario, based on the models given in Sect. 2, we can reduce the problem from Bessel functions to hyperbolic trigonometric functions cosh and sinh. The Laplacian in 3D spherical coordinates (spherically symmetric) becomes

$$\nabla^2 u = \frac{1}{r^2}\frac{\partial}{\partial r}\left(r^2\frac{\partial u}{\partial r}\right). \tag{29}$$

Step 1: Construct the concentration c

The corresponding governing equation for the concentration c in 3D spherical coordinates (spherically symmetric) is (2.26) in [10]:

$$\begin{cases} -\dfrac{1}{r^2}\partial_r(r^2\partial_r c) + \lambda c = 0 \quad \text{for } r \leqslant R(t), \\ c = c_B \quad \text{for } r \geqslant R(t). \end{cases} \tag{30}$$

Since $u(r,\theta,\phi)$ is independent of θ and ϕ, expanding the right-hand side of (29) yields

$$\nabla^2 u = \frac{2}{r}\frac{\partial u}{\partial r} + \frac{\partial^2 u}{\partial r^2}. \tag{31}$$

This is shown to be the same as $\frac{1}{r}\left(\frac{\partial^2}{\partial r^2}(ru)\right)$ by expanding this out using the product rule:

$$\frac{1}{r}\left(\frac{\partial^2}{\partial r^2}(ru)\right) = \frac{2}{r}\frac{\partial u}{\partial r} + \frac{\partial^2 u}{\partial r^2}. \tag{32}$$

Hence, we have

$$\frac{1}{r}\left(\frac{\partial^2}{\partial r^2}(ru)\right) = \lambda u. \tag{33}$$

Let $v = ru$. Then we obtain the general solution

$$\begin{aligned} &\frac{\partial^2 v}{\partial r^2} = \lambda v \\ &\Rightarrow v = C_1 \sinh(\sqrt{\lambda} r) + C_2 \cosh(\sqrt{\lambda} r) \\ &\Rightarrow u = \frac{1}{r}\Big(C_1 \sinh(\sqrt{\lambda} r) + C_2 \cosh(\sqrt{\lambda} r)\Big), \end{aligned} \tag{34}$$

where C_1 and C_2 are arbitrary constants, and this applies to odd dimensions. Further applying the BCs, we can solve this equation

$$c(r,t) = c_B \frac{R}{r} \frac{\sinh(\sqrt{\lambda} r)}{\sinh(\sqrt{\lambda} R)}. \tag{35}$$

Step 2: Construct the pressure p

We have the PDE for the pressure p:

$$\begin{cases} -\dfrac{1}{r^2}\partial_r(r^2 \partial_r p) = G_0 c \quad \text{for } r \leqslant R, \\ p = 0 \quad \text{for } r \geqslant R, \\ \dfrac{\mathrm{d}R}{\mathrm{d}t} = -\partial_r p(R), \\ \partial_r p(0) = 0, \end{cases} \tag{36}$$

and we can use $c(r,t)$ from (35) for $r \leqslant R$ obtained from Step 1.

We can combine the equations of the concentration (c) for $r \leqslant R(t)$ and the equation of the pressure (p) for $r \leqslant R(t)$, done similarly to Sect. 2, to obtain the Laplace's equation for $u = p + \frac{G_0}{\lambda} c$ as shown in (7), we have

$$\frac{\mathrm{d}^2 u}{\mathrm{d}r^2} + \frac{2}{r}\frac{\mathrm{d}u}{\mathrm{d}r} = 0. \tag{37}$$

This is a Cauchy-Euler (CE) equation, and thus we plug in the trial solution $u = r^s$, which gives

$$u = A_1(R) + A_2(R) r^{-1}, \tag{38}$$

where $A_1(R)$ and $A_2(R)$ are arbitrary constants. Since we require c, p to be bounded at the origin, $A_2(R)$ must be zero, so u must be constant in space, $u = A_1(R)$.

Then we can apply the BCs from (49), and determine the constant to be

$$p(r = R) = A_1(R) - \frac{G_0}{\lambda} c_B = 0 \qquad \Longrightarrow \qquad A_1(R) = \frac{G_0}{\lambda} c_B. \tag{39}$$

Therefore, we derive the final solution for the pressure p for the in vitro model:

$$p(r,t) = \frac{G_0 c_B}{\lambda}\left(1 - \frac{R \sinh(\sqrt{\lambda} r)}{r \sinh(\sqrt{\lambda} R)}\right). \tag{40}$$

Step 3: Construct the boundary velocity

Substituting the solution for p derived in (40) into the boundary velocity equation as in (9), we get the boundary velocity for the 3D spherically symmetric in vitro model is

$$\frac{\mathrm{d}R}{\mathrm{d}t} = G_0 c_B \left(-\frac{1}{\lambda R} + \frac{\cosh(\sqrt{\lambda} R)}{\sqrt{\lambda} \sinh(\sqrt{\lambda} R)}\right). \tag{41}$$

4.2 3D Spherically Symmetric Solution for the in Vivo Model

Step 1: Construct the concentration c

The equations for concentration in the in vivo model can be described as (2.31) in [10]

$$\begin{cases} -\dfrac{1}{r^2}\partial_r(r^2\partial_r c) + \lambda c = 0 \quad \text{for } r \leqslant R(t), \\ -\dfrac{1}{r^2}\partial_r(r^2\partial_r c) = c_B - c \quad \text{for } r \geqslant R(t). \end{cases} \tag{42}$$

We solve the above two equations and then apply the BCs, which ensure the continuity of both c and $\partial_r c$ at $R(t)$

$$\begin{cases} c^{(i)}(R,t) = c^{(o)}(R,t), \\ \partial_r c^{(i)}(R,t) = \partial_r c^{(o)}(R,t) \end{cases} \tag{43}$$

and we get

$$c(r,t) = \begin{cases} c_B a_0(R)\sinh(\sqrt{\lambda}r)/r \overset{\text{def}}{=} c^{(i)}(r,t) & \text{for } r \leqslant R(t), \\ c_B(b_0(R)\mathrm{e}^{-r} + r)/r \overset{\text{def}}{=} c^{(o)}(r,t) & \text{for } r \geqslant R(t), \end{cases} \tag{44}$$

where a_0 and b_0 are given by

$$a_0(R) = \frac{R+1}{\sqrt{\lambda}\cosh(\sqrt{\lambda}R) + \sinh(\sqrt{\lambda}R)}, \tag{45}$$

$$b_0(R) = -\frac{\sqrt{\lambda}\,R\cosh(\sqrt{\lambda}R) - \sinh(\sqrt{\lambda}R)}{-R(\sqrt{\lambda}\cosh(\sqrt{\lambda}R) + \sinh(\sqrt{\lambda}R))}. \tag{46}$$

The concentration for $r \leqslant R(t)$ in (44) is clear with the same form as (35), so we will not go into details. However, for the concentration when $r \geqslant R(t)$ as specified in (44), our analysis begins with the second equation of the in vivo model for regions where $r \geqslant R(t)$, as described in (42):

$$-\frac{1}{r^2}\frac{\partial}{\partial r}\left(r^2\frac{\partial c}{\partial r}\right) = c_B - c. \tag{47}$$

This equation simplifies upon substituting $v = rc$, which isolates the spatial component and transforms the PDE into an ODE:

$$-\frac{1}{r}\frac{\mathrm{d}^2 v}{\mathrm{d}r^2} = c_B - \frac{v}{r}. \tag{48}$$

Considering the homogeneous part first:

$$\frac{\mathrm{d}^2 v}{\mathrm{d}r^2} = v.$$

Assuming a trial solution $v = \mathrm{e}^{sr}$, we find

$$s^2\mathrm{e}^{sr} = \mathrm{e}^{sr} \quad \Rightarrow \quad s^2 = 1 \quad \Rightarrow \quad s = \pm 1.$$

Thus, the general solution for the homogeneous equation is

$$v_{\text{hom}} = B_1\mathrm{e}^{r} + B_2\mathrm{e}^{-r}.$$

Considering the requirement that c must be finite as $r \to \infty$, we set $B_1 = 0$, giving us $v_{\text{hom}} = B_2\mathrm{e}^{-r}$. Transforming back to c, the homogeneous solution is $c_{\text{hom}} = B_2\mathrm{e}^{-r}/r$.

Introducing a constant solution $c = c_B$ for the particular solution and combining, we have

$$c = \frac{B_2 \mathrm{e}^{-r}}{r} + c_B.$$

Renaming B_2 as b_0, the solution for $r \geqslant R(t)$ becomes

$$c(r,t) = c_B \left(b_0 \frac{\mathrm{e}^{-r}}{r} + 1 \right), \quad r \geqslant R(t),$$

which give us the concentration for $r \geqslant R(t)$ in (44).

Step 2: Construct the pressure p

We have the PDE for the pressure p:

$$\begin{cases} -\frac{1}{r^2}\partial_r(r^2 \partial_r p) = G_0 c \quad \text{for } r \leqslant R(t), \\ p = 0 \quad \text{for } r \geqslant R(t), \\ \frac{\mathrm{d}R}{\mathrm{d}t} = -\partial_r p(R), \\ \partial_r p(0) = 0 \end{cases} \tag{49}$$

as in (49), and we use the solution for the concentration c as in (44) and (45).

We arrive at the Laplace's equation for $u = p + \frac{G_0}{\lambda} c$, done similarly to Sect. 2, as shown in (7):

$$\frac{\mathrm{d}^2 u}{\mathrm{d}r^2} + \frac{2}{r}\frac{\mathrm{d}u}{\mathrm{d}r} = 0. \tag{50}$$

This is a CE equation, and using the same approach as in (38), we derive the general solution for the pressure $p = B_1(R) - \frac{G_0}{\lambda} c$. We then apply the BC:

$$\begin{aligned} & p(r = R) = B_1(R) - \frac{G_0}{\lambda} c(R) = B_1(R) - \frac{G_0}{\lambda} c_B = 0 \\ \Rightarrow\ & B_1(R) = \frac{G_0 c_B}{\lambda} \frac{a_0(R)}{R} \sinh(\sqrt{\lambda} R) = \frac{G_0 c_B}{\lambda}. \end{aligned} \tag{51}$$

Therefore, the solution for the pressure p for the in vivo model is

$$p(r,t) = B_1(R) - \frac{G_0}{\lambda} c = \frac{G_0 c_B}{\lambda} \frac{a_0(R)}{R} (\sinh(\sqrt{\lambda} R) - \sinh(\sqrt{\lambda} r)), \tag{52}$$

where a_0 is shown in (45).

Step 3: Construct the boundary velocity

Substituting the solution for p we derived in (52) into the boundary velocity equation as in (9), we get the boundary velocity for the 3D spherically symmetric in vivo model:

$$\frac{\mathrm{d}R}{\mathrm{d}t} = \frac{G_0 c_B}{\lambda} \frac{R+1}{R^2} \frac{\lambda R \cosh(\sqrt{\lambda} R) - \sqrt{\lambda} \sinh(\sqrt{\lambda} R)}{\lambda \cosh(\sqrt{\lambda} R) + \sqrt{\lambda} \sinh(\sqrt{\lambda} R)}. \tag{53}$$

Following (41) and (53), we plot the comparison of the tumor evolution speed for in vitro and in vivo models as shown in Figs. 6 and 7, where we can observe that the tumor in the in vivo model is growing slower than the in vitro model.

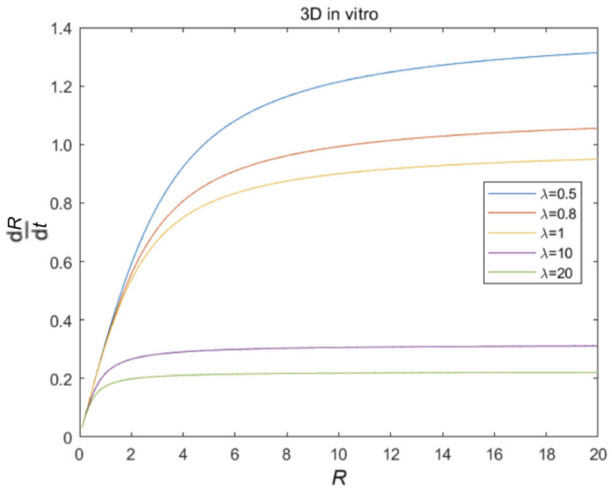

Fig. 6 3D in vitro tumor evolution (41)

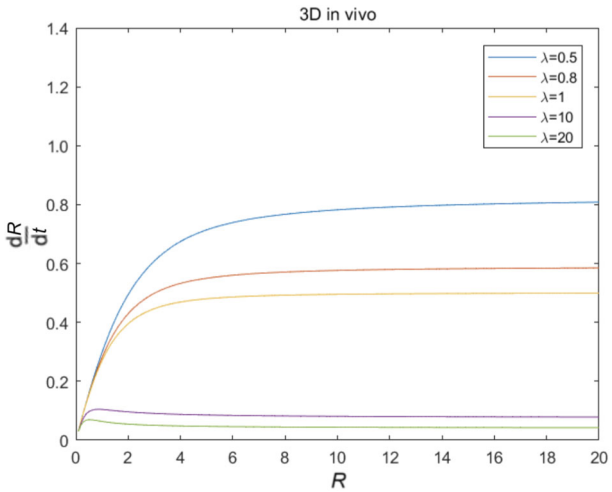

Fig. 7 3D in vivo tumor evolution (53)

4.3 Stability of 3D Spherically Symmetric in the in Vitro Model

Building upon the nutrient concentration PDEs outlined in (10), we now extend our analysis to the spherically symmetric 3D scenario:

$$-\nabla^2 c(r,\theta,\phi,t) + \lambda c(r,\theta,\phi,t) = 0 \quad \text{in} \quad \tilde{D}. \tag{54}$$

The 3D Laplacian in the spherical coordinate (r,θ,ϕ) is

$$\nabla^2 c = c_{rr} + \frac{2}{r}c_r + \frac{1}{r^2}\left[\frac{1}{\sin^2\theta}c_{\phi\phi} + \frac{1}{\sin\theta}(\sin\theta c_\theta)_\theta\right]. \tag{55}$$

The spherical harmonic function plays an important role in the 3D stability analysis. The spherical harmonic function of degree ℓ and order m is given by

$$Y_\ell^m(\theta,\phi)=\sqrt{\frac{2\ell+1}{4\pi}\frac{(\ell-m)!}{(\ell+m)!}}P_\ell^m(\cos\theta)\mathrm{e}^{\mathrm{i}m\phi}. \tag{56}$$

Here, ℓ can take on any noninteger values, and for each value of ℓ, m can range from $-\ell$ to ℓ. $P_\ell^m(\cos\theta)$ represents the associated Legendre polynomial. Note that $m=0$ mode corresponds to the unperturbed, spherically symmetric scenario. The stability analysis includes all modes, thereby generalizing to cases where $m=1,2,3,\cdots$. Consequently, this analysis involves the associated Legendre polynomial $P_\ell^m(\cos\theta)$.

Recall the asymptotic expansions for the perturbed solutions $\tilde{c}$ and $\tilde{p}$ after extending our analysis to three dimensions:

$$\begin{cases}\tilde{c}(r,\theta,\phi,t)=c_0(r,t)+\delta\tilde{c}_1(r,\theta,\phi,t)+O(\delta^2),\\ \tilde{p}(r,\theta,\phi,t)=p_0(r,t)+\delta\tilde{p}_1(r,\theta,\phi,t)+O(\delta^2).\end{cases} \tag{57}$$

Here, $c_0(r,t)$ and $p_0(r,t)$ are the leading-order solutions in the spherical coordinates (r,θ,ϕ), as we obtained in Sects. 4.1 and 4.2. These solutions describe the unperturbed, spherically symmetric case and depend only on the radial coordinate r and time t. The terms $\tilde{c}_1(r,\theta,\phi,t)$ and $\tilde{p}_1(r,\theta,\phi,t)$ represent the first-order terms, which include the additional angular dependence on θ and ϕ due to the introduced perturbations.

Consider the concentration $\tilde{c}_1(r,\theta,\phi,t)$ in the 3D spherical tumor model after perturbation. By applying separation of variables, we can express $\tilde{c}_1$ as a sum over radial functions and spherical harmonics, which respectively capture the radial and angular dependencies:

$$\tilde{c}_1=\sum_{\ell=0}^{\infty}\sum_{m=-\ell}^{\ell}c_{1\ell m}(r,t)Y_\ell^m(\theta,\phi). \tag{58}$$

Here, $c_{1\ell m}(r,t)$ represents the radial component of the concentration and depends only on the radial coordinate r and time t. The $Y_\ell^m(\theta,\phi)$ are spherical harmonics as introduced in (56), reflecting the dependence of the solution on the angular coordinates θ and ϕ. Based on this separation of variables from the linearized equation at $O(\delta)$, the BCs allow us to drop all $O(\delta^2)$ and smaller terms, which considerably simplifies the expansion. Therefore, for clarity and simplicity in the following discussions, we will use c_1 to represent $c_{1\ell m}(r,t)$. It is crucial to note that this representation of c_1 differs from the $c_1(r,\theta,\phi,t)$ obtained in the asymptotic expansion discussed in (57).

Based on the BC in (10), and evaluating the perturbed solution at the perturbed boundary point as in (21) using the asymptotic expansion in (57) after the separation of variables in (58), we have

$$\partial_r c_0(R(t),t)+c_1(R(t),t)=0. \tag{59}$$

Step 1: Construct the concentration c

The 3D Laplacian is therefore

$$\begin{aligned}\nabla^2\tilde{c}_1(r,\theta,\phi,t)=&(c_1)_{rr}Y_\ell^m(\theta,\phi)+\frac{2}{r}(c_1)_rY_\ell^m(\theta,\phi)\\&+\frac{c_1}{r^2}\left[\frac{1}{\sin^2\theta}\frac{\partial^2Y_\ell^m(\theta,\phi)}{\partial^2\phi}+\frac{1}{\sin\theta}\partial_\theta\left(\sin\theta\frac{\partial Y_\ell^m(\theta,\phi)}{\partial\phi}\right)\right],\end{aligned} \tag{60}$$

where c_1 on the right-hand side is the radial part $c_{1\ell m}(r,t)$. Substituting (56) into the above 3D Laplacian in the spherical coordinate, and since

$$\frac{\mathrm{d}}{\mathrm{d}\theta}\left(\sin\theta\frac{\mathrm{d}c}{\mathrm{d}\theta}\right) = -\left(\mu\sin\theta - \frac{\gamma}{\sin\theta}\right)c_1 Y_\ell^m(\theta,\phi), \tag{61}$$

where $\mu = \ell(\ell+1)$ and $\gamma = m^2$. Following these, we have

$$\begin{aligned}\nabla^2 c_1(r,\theta,\phi) =& (c_1)_{rr}Y_\ell^m(\theta,\phi) + \frac{2}{r}(c_1)_r Y_\ell^m(\theta,\phi)\\ &+ \frac{c_1}{r^2}\left(\frac{1}{\sin^2\theta}(-m^2)Y_\ell^m(\theta,\phi) + \frac{1}{\sin\theta}\left(-\mu\sin\theta + \frac{\gamma}{\sin\theta}\right)Y_\ell^m(\theta,\phi)\right)\\ =& \left((c_1)_{rr} + \frac{2}{r}(c_1)_r - \frac{\mu}{r^2}c_1\right)Y_\ell^m(\theta,\phi).\end{aligned} \tag{62}$$

Therefore, plugging (62) into (6) gives us

$$\begin{aligned}&-\nabla^2 c + \lambda c = 0\\ &\Rightarrow -\left((c_1)_{rr} + \frac{2}{r}(c_1)_r - \frac{\mu}{r^2}c_1\right)Y_\ell^m(\theta,\phi) + \lambda c_1 Y_\ell^m(\theta,\phi) = 0\\ &\Rightarrow r^2(c_1)_{rr} + 2r(c_1)_r - (\lambda r^2 + \mu)c_1 = 0,\end{aligned} \tag{63}$$

where $\mu = \ell(\ell+1)$, and since the standard form of the modified spherical Bessel equation of order n is

$$x^2\frac{\mathrm{d}^2 y}{\mathrm{d}x^2} + 2x\frac{\mathrm{d}y}{\mathrm{d}x} - (x^2 + n(n+1))y = 0. \tag{64}$$

We can convert

$$r^2(c_1)_{rr} + 2r(c_1)_r - (\lambda r^2 + \mu)c_1 = 0 \tag{65}$$

to the standard form by change of variables, namely, $c_1(r) = y(z)/\sqrt{z}$ with $z = \sqrt{\lambda}r$. Therefore, the solution to (65) is

$$y(z) = C_1 I_w(z) + C_2 K_w(z), \tag{66}$$

where $w = \ell + \frac{1}{2}$. Since the solution is bounded at $z = 0$, which sets $C_2 = 0$,

$$c_1(r) = \frac{C_1 I_{\ell+\frac{1}{2}}(\sqrt{\lambda}r)}{\sqrt{\sqrt{\lambda}r}}. \tag{67}$$

Given the BCs:

$$\partial_r c_0(R(t),t) + c_1(R(t),t) = 0. \tag{68}$$

Thus from (68) and substituting in the derived result for c_0 from (35), we obtain

$$c_1(R(t),t) = -\frac{c_B\sqrt{\lambda}\cosh(\sqrt{\lambda}R)}{\sinh(\sqrt{\lambda}R)}.$$

By using the BCs in (59), we have

$$-\frac{c_B\sqrt{\lambda}\cosh(\sqrt{\lambda}R)}{\sinh(\sqrt{\lambda}R)} = C_1\frac{I_{\ell+\frac{1}{2}}(\sqrt{\lambda}R)}{\sqrt{\sqrt{\lambda}R}}. \tag{69}$$

Therefore, for the in vitro model, we have the concentration inside the tumor:

$$c_1(r,t) = c_B a_1(t) \frac{I_{\ell+\frac{1}{2}}(\sqrt{\lambda}r)}{\sqrt{\sqrt{\lambda}r}} \tag{70}$$

and the leading-order term $c_0(r,t)$ for this case is given by (68). Rename C_1 as a_1, and we have

$$a_1(R(t)) = -\frac{\sqrt{\lambda}\cosh(\sqrt{\lambda}R)\sqrt{\sqrt{\lambda}R}}{\sinh(\sqrt{\lambda}R) I_{\ell+\frac{1}{2}}(\sqrt{\lambda}R)}. \tag{71}$$

The concentration outside the tumor is the constant c_B.

Step 2: Construct pressure p_1

The PDE for the pressure p is

$$-\nabla^2 p_1(r,\theta,\phi,t) = G_0 c_1(r,\theta,\phi,t) \text{ in } \tilde{D}(t) \tag{72}$$

with BC

$$\partial_r p_0(R(t),t) + p_1(R(t),t) = 0. \tag{73}$$

Since $-\nabla^2 c_1(r,\theta,\phi,t) + \lambda c_1(r,\theta,\phi,t) = 0$, meaning that $c_1 = \frac{1}{\lambda}\nabla^2 c_1$, therefore

$$\begin{cases} -\nabla^2 p_1(r,\theta,\phi,t) = G_0 c_1(r,\theta,\phi,t), \\ -\nabla^2 p_1 - \dfrac{G_0}{\lambda}\nabla^2 c_1 = 0. \end{cases} \tag{74}$$

Then we substitute the Laplacian in the 3D spherical coordinate for the pressure p, combining the pressure and concentration equations as in (7), which gives us the Laplace's equation for $u_1 = p_1 + \frac{G_0}{\lambda}c_1$. Since we have the Laplace operator after perturbation as in (62), we have

$$r^2 \frac{\mathrm{d}^2 u_1}{\mathrm{d}r^2} + 2r\frac{\mathrm{d}u_1}{\mathrm{d}r} - \ell(\ell+1)u_1 = 0. \tag{75}$$

This is in the CE form, and has the general solution

$$u = H_1 r^{\ell} + H_2 r^{-\ell}. \tag{76}$$

Since the solution is bounded, hence we get

$$u = H_1(R) r^{\ell}. \tag{77}$$

We then apply the BCs in (73), and substitute p_0 as in (40), and we obtain

$$p_1(R,t) = \frac{G_0 c_B}{\lambda}\left(-\frac{1}{R} + \frac{\sqrt{\lambda}\cosh(\sqrt{\lambda}R)}{\sinh(\sqrt{\lambda}R)}\right). \tag{78}$$

Since $p_1 = u_1 - G_0 c_1/\lambda$, we have

$$p_1(R,t) = H_1 R^{\ell} - \frac{G_0}{\lambda} c_1(R), \tag{79}$$

where $c_1(R)$ can be derived by plugging $r = R$ into (70) with (71).

We combine (78) and (79), and substitute (70) for $c_1(R(t), t)$ in the above equation to solve for $H_1(R)$, and we get

$$H_1(R) = R^{-\ell}\left[\left(\frac{RG_0c_B\sinh(\sqrt{\lambda}r)}{r^2\lambda\sinh(\sqrt{\lambda}R)} - \frac{RG_0c_B\cosh(\sqrt{\lambda}r)}{r\sqrt{\lambda}\sinh(\sqrt{\lambda}R)}\right) - \frac{G_0}{\lambda}\left(\frac{c_B\sqrt{\lambda}\cosh(\sqrt{\lambda}R)}{\sinh(\sqrt{\lambda}R)}\right)\right]$$

$$\Rightarrow H_1(R) = -R^{-\ell-1}\left(\frac{G_0c_B\sinh(\sqrt{\lambda}R)}{\lambda\sinh(\sqrt{\lambda}R)}\right) = -R^{-\ell-1}\left(\frac{G_0c_B}{\lambda}\right). \tag{80}$$

We then substitute (80) into (79), and we get the solution for p_1:

$$p_1(r,t) = -\frac{G_0c_B}{\lambda}\left(-\frac{r^\ell}{R^{\ell+1}} + \frac{\sqrt{\lambda}\cosh(\sqrt{\lambda}R)\sqrt{R}}{\sinh(\sqrt{\lambda}R)I_{\ell+\frac{1}{2}}(\sqrt{\lambda}R)}\frac{I_{\ell+\frac{1}{2}}(\sqrt{\lambda}r)}{\sqrt{r}}\right). \tag{81}$$

Step 3: Construct $\delta^{-1}\frac{\mathrm{d}\delta}{\mathrm{d}t}$

From the previous perturbation analysis we have the evolution function

$$\delta^{-1}\frac{\mathrm{d}\delta}{\mathrm{d}t} = -(\partial_r^2 p_0(R,t) + \partial_r p_1(R,t)). \tag{82}$$

We substitute $p_0(R) = -\frac{G_0}{\lambda}\frac{1}{r}\frac{c_BR\sinh(\sqrt{\lambda}R)}{\sinh(\sqrt{\lambda}R)} + \frac{G_0c_B}{\lambda}$ and p_1 as in (81), so we get

$$\begin{aligned}\delta^{-1}\frac{\mathrm{d}\delta}{\mathrm{d}t} =& \frac{Rc_BG_0I_{\ell+\frac{1}{2}}(\sqrt{\lambda}R)R^{-1-\ell}\sinh(\sqrt{\lambda}R)R^{\ell+\frac{5}{2}}\ell\sqrt{\lambda}}{\lambda^{3/2}R^{7/2}\sinh(\sqrt{\lambda}R)I_{\ell+\frac{1}{2}}(\sqrt{\lambda}R)}\\ &+ \frac{Rc_BG_0I_{\ell+\frac{1}{2}}(\sqrt{\lambda}R)(2\sqrt{\lambda}\sqrt{R}+\lambda^{3/2}R^{5/2})\sinh(\sqrt{\lambda}R)}{\lambda^{3/2}R^{7/2}\sinh(\sqrt{\lambda}R)I_{\ell+\frac{1}{2}}(\sqrt{\lambda}R)}\\ &- \frac{2Rc_BG_0I_{\ell+\frac{1}{2}}(\sqrt{\lambda}R)\cosh(\sqrt{\lambda}R)\lambda R^{3/2}}{\lambda^{3/2}R^{7/2}\sinh(\sqrt{\lambda}R)I_{\ell+\frac{1}{2}}(\sqrt{\lambda}R)}\\ &- \frac{(-\lambda(\ell+1)I_{\ell+\frac{1}{2}}(\sqrt{\lambda}R)+I_{\ell-\frac{1}{2}}(\sqrt{\lambda}R)\lambda^{3/2}R)R^{5/2}\cosh(\sqrt{\lambda}R)}{2\lambda^{3/2}R^{7/2}\sinh(\sqrt{\lambda}R)I_{\ell+\frac{1}{2}}(\sqrt{\lambda}R)}\\ \overset{\text{def}}{=}& M_1(\lambda,\ell,R).\end{aligned} \tag{83}$$

Step 4: Boundary stability analysis

The goal is to determine the sign of the evolution function $\delta^{-1}\frac{\mathrm{d}\delta}{\mathrm{d}t}$, and then determine the stability of the tumor boundary. By substituting the asymptotic expansions for the modified Bessel functions and the hyperbolic functions as in Appendix A, we arrive at (111) in Sect. 5, which are summarized as Corollary 1 and indicate the negative sign of the evolution function in the 3D in vitro scenario. From Figs. 8, 9 below, we can also see that the evolution function $\delta^{-1}\frac{\mathrm{d}\delta}{\mathrm{d}t} < 0$ is always true, meaning that in the 3D in vitro model, the perturbation will degenerate and the tumor boundary will always become stable.

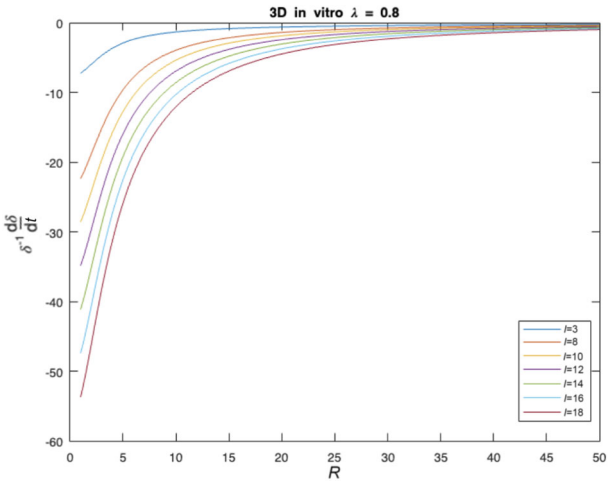

Fig. 8 3D in vitro $\lambda = 0.8$, $\ell = 3, 8, 10, 12, 14, 16, 18$

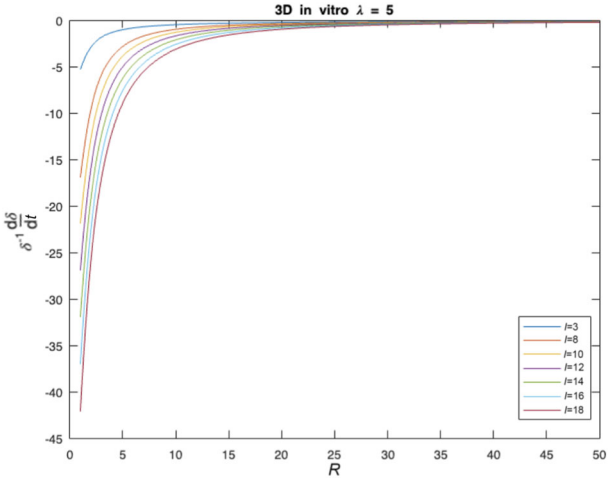

Fig. 9 3D in vitro $\lambda = 5$, $\ell = 3, 8, 10, 12, 14, 16, 18$

4.4 Stability of 3D Spherically Symmetric in the in Vivo Model

The PDEs for the 3D in vivo problem is

$$\begin{cases} -\nabla^2 c_1^{(i)}(r,\theta,t) + \lambda c_1^{(i)}(r,\theta,t) = 0, \\ -\nabla^2 c_1^{(o)}(r,\theta,t) + c_1^{(o)}(r,\theta,t) = 0 \end{cases} \tag{84}$$

with the solution of the concentration $(c_1^{(i)}(0,t))$ bounded everywhere, the BCs and ICs:

$$\begin{cases} c_1^{(o)}(\infty,t)=0, \\ c_1^{(i)}(R(t),t)=c_1^{(o)}(R(t),t), \\ \partial_r c_1^{(i)}(R(t),t)=\partial_r c_1^{(o)}(R(t),t), \\ \partial_r^2 c_0^{(i)}(R(t),t)+\partial_r c_1^{(i)}(R(t),t)=\partial_r^2 c_0^{(o)}(R(t),t)+\partial_r c_1^{(o)}(R(t),t). \end{cases} \tag{85}$$

Step 1: Construct the concentration c

For the in vivo model, the idea is to plug the expansion as in (58) into (84), where $\mu=\ell(\ell+1)$, $\gamma=m^2$. The construction for the concentration inside the tumor $c^{(i)}(r,t)$ is exactly the same as that in the in vitro model when solving $c(r,t)$, and thus we skip the construction of $c^{(i)}(r,t)$ and arrive at the general solution

$$c^{(i)}(r,t)=C_1\frac{I_{\ell+\frac{1}{2}}(\sqrt{\lambda}r)}{\sqrt{\sqrt{\lambda}r}}. \tag{86}$$

Then we consider the concentration outside the tumor $c^{(o)}(r,t)$ governed by the second equation in (84) and since we have $\nabla^2 c_1(r,\theta,\phi)=r^2(c1)_{rr}+2r(c_2)_r-\mu c_1$ as derived in (62), we get

$$\begin{aligned} &\Rightarrow \left[r^2(c_1)_{rr}+2r(c_1)_r-\left(\frac{m^2}{r^2\sin^2\theta}+\frac{\mu}{r^2}-\frac{\gamma}{r^2\sin^2\theta}+1\right)c_1\right]Y_\ell^m(\theta,\phi)=0 \\ &\Rightarrow r^2(c_1)_{rr}+2r(c_1)_r-(r^2+\mu)c_1=0, \end{aligned} \tag{87}$$

where $\mu=\ell(\ell+1)$, and since the standard form for the modified spherical Bessel function is as in (64), and we can convert (65) to the standard form by change of variables, namely, $c(r)=y(r)/\sqrt{r}$. Therefore, the solution to the governing equation for concentration outside the tumor is

$$c^{(o)}(r,t)=C_3\frac{I_\nu(r)}{\sqrt{r}}+C_4\frac{K_\nu(r)}{\sqrt{r}}, \tag{88}$$

where $\nu=\ell+\frac{1}{2}$ as before. Since I_ν blows up when $r\to\infty$, $C_3=0$, and the general solution becomes

$$c^{(o)}(r,t)=C_4\frac{K_\nu(r)}{\sqrt{r}}. \tag{89}$$

Then we apply the BCs as in (85) to get the constants C_1, C_4 and write in a consistent form. Hence, for any $k\in\mathbb{N}^+$ we have

$$c_1^{(i)}(r,t)=c_B a_1(t)\frac{I_{\ell+\frac{1}{2}}(\sqrt{\lambda}r)}{\sqrt{\sqrt{\lambda}r}}\quad \text{for } r\leqslant R(t), \tag{90}$$

$$c_1^{(o)}(r,t)=c_B b_1(t)\frac{K_{\ell+\frac{1}{2}}(r)}{\sqrt{r}}\quad \text{for } r\geqslant R(t). \tag{91}$$

Recall that the leading-order terms $c_0^{(i)}(\xi)$ and $c_0^{(o)}(\xi)$ are given by (44) and (45). Then applying the BCs (85) yields

$$a_1(t) = \frac{(((R+1)\lambda^{3/2} - \sqrt{\lambda})\sinh(\sqrt{\lambda}R) + \cosh(\sqrt{\lambda}R)R\lambda)(\sqrt{\lambda}R)^{3/2}K_{\ell+\frac{1}{2}}(R)}{\lambda R C(R)}, \tag{92}$$

$$b_1(t) = \frac{2(((R+1)\lambda^{3/2} - \sqrt{\lambda})\sinh(\sqrt{\lambda}R) + \cosh(\sqrt{\lambda}R)R\lambda)I_{\ell+\frac{1}{2}}(\sqrt{\lambda}R)}{2C(R)}, \tag{93}$$

where

$$\begin{aligned} C(R) = {} & (\sqrt{\lambda}\cosh(\sqrt{\lambda}R) + \sinh(\sqrt{\lambda}R))\left(K_{\ell-\frac{1}{2}}(R)R - \frac{K_{\ell+\frac{1}{2}}(R)}{2}\right)I_{\ell+\frac{1}{2}}(\sqrt{\lambda}R) \\ & + RI_{\ell-\frac{1}{2}}(\sqrt{\lambda}R)K_{\ell+\frac{1}{2}}(R)(\cosh(\sqrt{\lambda}R)\lambda + \sinh(\sqrt{\lambda}R)\sqrt{\lambda}). \end{aligned} \tag{94}$$

Step 2: Construct pressure p_1

By now, $c_1(r,t)$ is determined, therefore, $c_1(r,\theta,\phi)$ is also determined. Then, by solving the equation for the pressure p:

$$-\nabla^2 p_1(r,\theta,\phi,t) = G_0 c_1(r,\theta,\phi,t) \ \text{ in } \ \tilde{D}(t) \tag{95}$$

with the BC

$$\partial_r p_0(R(t),t) + p_1(R(t),t) = 0, \tag{96}$$

and expansion $p_1(r,\theta,t) = p_1(r,t)Y_\ell^m(\theta,\phi)$ and p_0 given by (52), we can solve for p_1.

Specifically, since $-\nabla^2 c_1(r,\theta,\phi,t) + \lambda c_1(r,\theta,\phi,t) = 0$, meaning that $c_1 = \frac{1}{\lambda}\nabla^2 c_1$, therefore

$$\begin{cases} -\nabla^2 p_1(r,\theta,\phi,t) = G_0 c_1(r,\theta,\phi,t), \\ -\nabla^2 p_1 - \dfrac{G}{\lambda}\nabla^2 c_1 = 0. \end{cases} \tag{97}$$

Then we substitute the Laplacian in the 3D spherical coordinate for the pressure p, combining the pressure and concentration equations as in (7), which gives us the Laplace's equation for $u_1 = p_1 + \frac{G}{\lambda}c_1$. Since we have the Laplace operator after perturbation as in (62), we have

$$r^2\frac{\mathrm{d}^2 u_1}{\mathrm{d}r^2} + 2r\frac{\mathrm{d}u_1}{\mathrm{d}r} - \mu u_1 = 0. \tag{98}$$

This is in the CE form, and has the general solution $u_1 = D_1(R)r^\ell + D_2(R)r^{-\ell}$, since the solution is bounded at the origin, $D_2(R) = 0$, and we have $u_1 = D_1(R)r^\ell$.

By applying the BCs and substituting p_0 as in (52) and a_0 given in (45). Therefore,

$$\begin{aligned} p_1(R(t),t) &= -\partial_r p_0(R(t),t) \\ &= \frac{G_0 c_B}{\lambda}\frac{R+1}{R^2}\frac{\lambda R\cosh(\sqrt{\lambda}R) - \sqrt{\lambda}\sinh(\sqrt{\lambda}R)}{\lambda\cosh(\sqrt{\lambda}R) + \sqrt{\lambda}\sinh(\sqrt{\lambda}R)}, \end{aligned} \tag{99}$$

and since $p_1(R,t) = u_1(R) - G_0 c_1/\lambda$, we have

$$p_1(R,t) = D_1(R)R^\ell - \frac{G_0}{\lambda}c_1(R). \tag{100}$$

We combine (99) and (100), and substitute (90) for $c_1^{(i),1}(R(t),t)$ in the above equation to solve for constant $D_1(R)$. We get

$$D_1(R) = \frac{G_0 c_B}{\lambda}\left(\frac{R+1}{R^{2+\ell}}\frac{\lambda R\cosh(\sqrt{\lambda}R) - \sqrt{\lambda}\sinh(\sqrt{\lambda}R)}{\lambda\cosh(\sqrt{\lambda}R) + \sqrt{\lambda}\sinh(\sqrt{\lambda}R)} + \frac{a_1}{R^\ell}\frac{I_{\ell+\frac{1}{2}}(\sqrt{\lambda}R)}{\sqrt{\sqrt{\lambda}R}}\right), \tag{101}$$

where b_1 is shown in (93).

We then substitute (101) and (93) into (100), and we get the solution for p_1 for the in vivo model

$$p_1(t) = \frac{G_0 c_B}{\lambda}\left[\left(\frac{R+1}{R^{2+\ell}}\frac{\lambda R\cosh(\sqrt{\lambda}R) - \sqrt{\lambda}\sinh(\sqrt{\lambda}R)}{\lambda\cosh(\sqrt{\lambda}R) + \sqrt{\lambda}\sinh(\sqrt{\lambda}R)} + \frac{a_1}{R^\ell}\frac{I_{\ell+\frac{1}{2}}(\sqrt{\lambda}R)}{\sqrt{\sqrt{\lambda}R}}\right) r^\ell - a_1\frac{I_{\ell+\frac{1}{2}}(\sqrt{\lambda}R)}{\sqrt{\sqrt{\lambda}R}}\right], \tag{102}$$

where a_1 is shown in (92).

Step 3: Construct $\delta^{-1}\frac{\mathrm{d}\delta}{\mathrm{d}t}$

Since we have the expression for the evolution function $\delta^{-1}\frac{\mathrm{d}\delta}{\mathrm{d}t}$:

$$\delta^{-1}\frac{\mathrm{d}\delta}{\mathrm{d}t} = -(\partial_r^2 p_0(R,t) + \partial_r p_1(R,t)) \tag{103}$$

with

$$p_0(r,t) = \frac{-G_0 c_B}{\lambda}\left(\frac{a_0(R)\sinh(\sqrt{\lambda}r)}{r} + \frac{a_0(R)\sinh(\sqrt{\lambda}R)}{R}\right), \tag{104}$$

where a_0 is constructed in (45), and p_1 is constructed as in (102).

We substitute them into (103), which gives us

$$\delta^{-1}\frac{\mathrm{d}\delta}{\mathrm{d}t} = \frac{T_1}{T_2} \overset{\text{def}}{=} M_2(\lambda, \ell, R), \tag{105}$$

where

$$\begin{aligned}
T_1 = &- G_0 c_B(((-2R((3R+2)\lambda^{3/2} + \sqrt{\lambda}(R-2))(\ell+1/2)K_{\ell+\frac{1}{2}}(R) \\
&- 2(R(R-\ell/2-1)\lambda^{3/2} - \sqrt{\lambda}(\ell+2)(R-2)/2)(R+1)K_{\ell-\frac{1}{2}}(R)) \\
&\cdot \cosh(\sqrt{\lambda}R)^3 - 2\sinh(\sqrt{\lambda}R)(R(\ell+1/2)((\lambda^2+3\lambda)R + \lambda^2 - 1)K_{\ell+\frac{1}{2}}(R) \\
&+ ((\lambda^2+\lambda)R^2 - 2\lambda(\ell+2)R + (\lambda+1)(\ell+2))(R+1)K_{\ell-\frac{1}{2}}(R)/2) \\
&\cdot \cosh(\sqrt{\lambda}R)^2 + (2R((2R+2)\lambda^{3/2} + \sqrt{\lambda}(R-2))(\ell+1/2)K_{\ell+\frac{1}{2}}(R) \\
&+ 2(R^2\lambda^{3/2} - \sqrt{\lambda}(\ell+2)(R-2)/2)(R+1)K_{\ell-\frac{1}{2}}(R))\cosh(\sqrt{\lambda}R) \\
&+ 2\sinh(\sqrt{\lambda}R)(R(\ell+1/2)(\lambda R + \lambda - 1)K_{\ell+\frac{1}{2}}(R) \\
&+ K_{\ell-\frac{1}{2}}(R)(R+1)(R^2\lambda + \ell + 2)/2))I_{\ell+\frac{1}{2}}(\sqrt{\lambda}R) \\
&+ I_{\ell-\frac{1}{2}}(\sqrt{\lambda}R)(R^2 + (\ell+2)R + \ell + 2)(\lambda(-2 + (\lambda+1)R)\cosh(\sqrt{\lambda}R)^3 \\
&+ 2\sinh(\sqrt{\lambda}R)((R-1/2)\lambda^{3/2} - \sqrt{\lambda}/2)\cosh(\sqrt{\lambda}R)^2 \\
&- \lambda(R-2)\cosh(\sqrt{\lambda}R) + \sinh(\sqrt{\lambda}R)\sqrt{\lambda})K_{\ell+\frac{1}{2}}(R)
\end{aligned} \tag{106}$$

and

$$\begin{aligned} T_2 =& \sqrt{\lambda} R^3 K_{\ell+\frac{1}{2}}(R)(\cosh(\sqrt{\lambda}R)\lambda + \sinh(\sqrt{\lambda}R)\sqrt{\lambda}) I_{\ell-\frac{1}{2}}(\sqrt{\lambda}R) \\ &+ I_{\ell+\frac{1}{2}}(\sqrt{\lambda}R) K_{\ell-\frac{1}{2}}(R)(\sqrt{\lambda}\cosh(\sqrt{\lambda}R) + \sinh(\sqrt{\lambda}R))) \\ &\cdot (\cosh(\sqrt{\lambda}R)\lambda + \sinh(\sqrt{\lambda}R)\sqrt{\lambda})(\sqrt{\lambda}\cosh(\sqrt{\lambda}R) + \sinh(\sqrt{\lambda}R)). \end{aligned} \tag{107}$$

Step 4: Boundary stability analysis

We have the evolution function as in (105)–(110). To determine the sign of the evolution function, we can substitute the asymptotic expansions of the modified Bessel functions and the hyperbolic trigonometric functions when $r \to \infty$ and $r \to 0$. Specifically, in our analysis, we first substitute the given asymptotic expansions into the evolution function. This step is followed by simplifying the expression and arranging the terms in the descending order of powers of R. For the case when $r \to \infty$, we focus on the highest power term of R due to its dominance in the evolution function for large R values. We extract its coefficient as the key term. Conversely, when $r \to 0$, the lowest power term of R becomes significant. Here, we isolate this term from the evolution function after the substitution of the relevant asymptotic expansions and retrieve its coefficient. This analysis clarifies the behavior of the evolution function near zero and infinity, pivotal for determining the tumor boundary stability; a negative evolution function denotes the stability, whereas a positive evolution function indicates the instability. The results of this will be shown in Sect. 5.1.

5 Results and Discussion

5.1 Results for 3D Tumor Model

Theorem 1 *In the three dimensions, given the growing rate $G_0 > 0$, background concentration $c_B > 0$, nutrient consumption rate $\lambda > 0$, and perturbation degree ℓ and order m of the spherical harmonic function $Y_\ell^m(\theta, \phi)$ as in (56). If the radius of the tumor is around R, where the corresponding unperturbed tumor has radius R, the evolution function $\delta^{-1}\frac{\mathrm{d}\delta}{\mathrm{d}t}$ for the in vitro model is given by (83):*

$$\begin{aligned} \delta^{-1}\frac{\mathrm{d}\delta}{\mathrm{d}t} =& \frac{Rc_B G_0 I_{\ell+\frac{1}{2}}(\sqrt{\lambda}R) R^{-1-\ell}\sinh(\sqrt{\lambda}R) R^{\ell+\frac{5}{2}}\ell\sqrt{\lambda}}{\lambda^{3/2}R^{7/2}\sinh(\sqrt{\lambda}R) I_{\ell+\frac{1}{2}}(\sqrt{\lambda}R)} \\ &+ \frac{Rc_B G_0 I_{\ell+\frac{1}{2}}(\sqrt{\lambda}R)(2\sqrt{\lambda}\sqrt{R} + \lambda^{3/2}R^{5/2})\sinh(\sqrt{\lambda}R)}{\lambda^{3/2}R^{7/2}\sinh(\sqrt{\lambda}R) I_{\ell+\frac{1}{2}}(\sqrt{\lambda}R)} \\ &- \frac{2Rc_B G_0 I_{\ell+\frac{1}{2}}(\sqrt{\lambda}R)\cosh(\sqrt{\lambda}R)\lambda R^{3/2}}{\lambda^{3/2}R^{7/2}\sinh(\sqrt{\lambda}R) I_{\ell+\frac{1}{2}}(\sqrt{\lambda}R)} \\ &- \frac{(-\lambda(\ell+1) I_{\ell+\frac{1}{2}}(\sqrt{\lambda}R) + I_{\ell-\frac{1}{2}}(\sqrt{\lambda}R)\lambda^{3/2}R) R^{5/2}\cosh(\sqrt{\lambda}R)}{2\lambda^{3/2}R^{7/2}\sinh(\sqrt{\lambda}R) I_{\ell+\frac{1}{2}}(\sqrt{\lambda}R)} \\ \stackrel{\text{def}}{=}& M_1(\lambda, \ell, R) \end{aligned}$$

and for the in vivo model, it is given by (105):

$$\delta^{-1}\frac{\mathrm{d}\delta}{\mathrm{d}t}=\frac{T_1}{T_2}\overset{\text{def}}{=}M_2(\lambda,\ell,R), \tag{108}$$

where

$$\begin{aligned}
T_1 =& -G_0c_B(((-2R((3R+2)\lambda^{3/2}+\sqrt{\lambda}(R-2))(\ell+1/2)K_{\ell+\frac{1}{2}}(R)\\
&-2(R(R-\ell/2-1)\lambda^{3/2}-\sqrt{\lambda}(\ell+2)(R-2)/2)(R+1)K_{\ell-\frac{1}{2}}(R))\\
&\cdot\cosh(\sqrt{\lambda}R)^3-2\sinh(\sqrt{\lambda}R)(R(\ell+1/2)((\lambda^2+3\lambda)R+\lambda^2-1)K_{\ell+\frac{1}{2}}(R)\\
&+((\lambda^2+\lambda)R^2-2\lambda(\ell+2)R+(\lambda+1)(\ell+2))(R+1)K_{\ell-\frac{1}{2}}(R)/2)\\
&\cdot\cosh(\sqrt{\lambda}R)^2+(2R((2R+2)\lambda^{3/2}+\sqrt{\lambda}(R-2))(\ell+1/2)K_{\ell+\frac{1}{2}}(R)\\
&+2(R^2\lambda^{3/2}-\sqrt{\lambda}(\ell+2)(R-2)/2)(R+1)K_{\ell-\frac{1}{2}}(R))\cosh(\sqrt{\lambda}R)\\
&+2\sinh(\sqrt{\lambda}R)(R(\ell+1/2)(\lambda R+\lambda-1)K_{\ell+\frac{1}{2}}(R)\\
&+K_{\ell-\frac{1}{2}}(R)(R+1)(R^2\lambda+\ell+2)/2))I_{\ell+\frac{1}{2}}(\sqrt{\lambda}R)\\
&+I_{\ell-\frac{1}{2}}(\sqrt{\lambda}R)(R^2+(\ell+2)R+\ell+2)(\lambda(-2+(\lambda+1)R)\cosh(\sqrt{\lambda}R)^3\\
&+2\sinh(\sqrt{\lambda}R)((R-1/2)\lambda^{3/2}-\sqrt{\lambda}/2)\cosh(\sqrt{\lambda}R)^2\\
&-\lambda(R-2)\cosh(\sqrt{\lambda}R)+\sinh(\sqrt{\lambda}R)\sqrt{\lambda})K_{\ell+\frac{1}{2}}(R)
\end{aligned} \tag{109}$$

and

$$\begin{aligned}
T_2 =&\sqrt{\lambda}R^3K_{\ell+\frac{1}{2}}(R)(\cosh(\sqrt{\lambda}R)\lambda+\sinh(\sqrt{\lambda}R)\sqrt{\lambda})I_{\ell-\frac{1}{2}}(\sqrt{\lambda}R)\\
&+I_{\ell+\frac{1}{2}}(\sqrt{\lambda}R)K_{\ell-\frac{1}{2}}(R)(\sqrt{\lambda}\cosh(\sqrt{\lambda}R)+\sinh(\sqrt{\lambda}R)))\\
&\cdot(\cosh(\sqrt{\lambda}R)\lambda+\sinh(\sqrt{\lambda}R)\sqrt{\lambda})(\sqrt{\lambda}\cosh(\sqrt{\lambda}R)+\sinh(\sqrt{\lambda}R)).
\end{aligned} \tag{110}$$

Note that the scaling parameters $G_0, c_B > 0$ do not influence the quantitative behavior of $\delta^{-1}\frac{\mathrm{d}\delta}{\mathrm{d}t}$. Also, in our analysis, the wave number m is canceled out in (62). This is reasonable, considering that although m primarily specifies orientations or symmetries, the fundamental characteristics of the solutions are predominantly determined by the parameter ℓ. This is due to the dependency of m on ℓ, as indicated by the relationship $-\ell \leqslant m \leqslant \ell$. Essentially, it is the wave number ℓ that plays the central role in defining the nature of these solutions. For the in vitro model, we will show that $M_1(\lambda, \ell, R)$ is always negative, where they are shown in Figs. 8 and 9. For the in vivo model, fix the values of $G_0, c_B > 0$, $M_2(\lambda, \ell, R)$ is plotted in Figs. 10, 11, 12, 13, for a different choice of λ and perturbation parameter ℓ. Based on the expression of $\delta^{-1}\frac{\mathrm{d}\delta}{\mathrm{d}t}$ for the two nutrient models and the figures, we establish the following remarks.

Remark 3 $M_1(\lambda, 1, R) = M_2(\lambda, 1, R) = 0$ for any $\lambda, R > 0$, since the model 1 perturbation corresponds to a trivial translation instead of the change of the boundary geometry.

Remark 4 When $0 < \lambda < \lambda^*(\ell)$, fix any degree $\ell \leqslant 2$ and order $-\ell \leqslant m \leqslant \ell$ of the spherical harmonic function $Y_\ell^m(\theta, \phi)$ in the perturbation, $M_1(\lambda, 1, R)$ is always negative

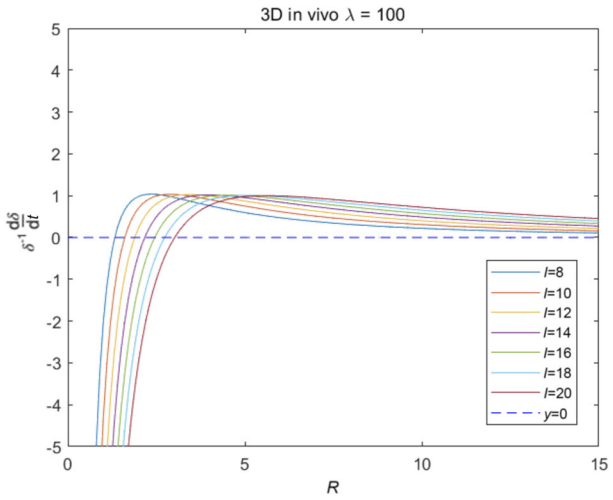

Fig. 10 3D in vivo, $G_0 = 1, c_B = 100, \lambda = 100, \ell = 8, 10, 12, 14, 16, 18, 20, R \in [0, 15]$

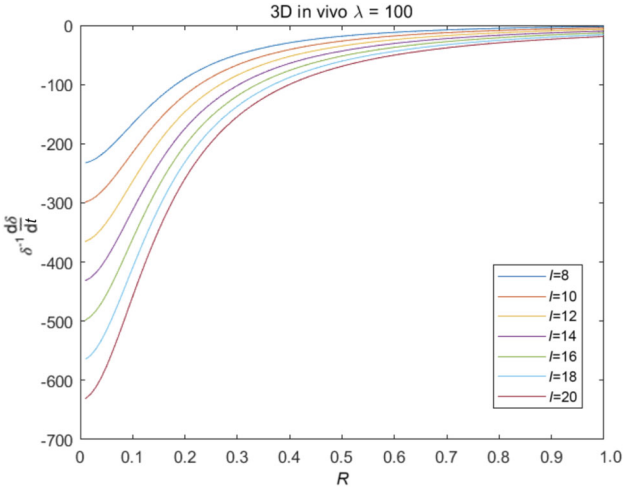

Fig. 11 3D in vivo, $G_0 = 1, c_B = 100, \lambda = 100, \ell = 8, 10, 12, 14, 16, 18, 20, R \in [0, 1]$

and monotone increases in R (see Figs. 10, 11, 12, 13). From a physical perspective, when the nutrient consumption rate λ is relatively low, the perturbation amplitude will continue to decrease to zero, where $\lambda^*(\ell)$ is the threshold of λ, and may be dependent on the wave number ℓ. This means that the tumor in this range will always evolve from an irregular shape to a regular shape like a sphere (with a larger size).

Remark 5 For the regime $\lambda \geqslant \lambda^*(\ell)$, we have the following.

i. There exists a threshold $R^*(\ell)$ such that $F_2(\lambda, 1, R) < 0$ for $0 < R < R^*(\ell)$, and $F_2(\lambda, 1, R) > 0$ for $R > R^*(\ell)$ (see Figs. 10, 11). This means considering the degree ℓ and the order m, and assuming the nutrient consumption rate is significant, the perturbation amplitude will degenerate for tumors with a small radius, and increase when the

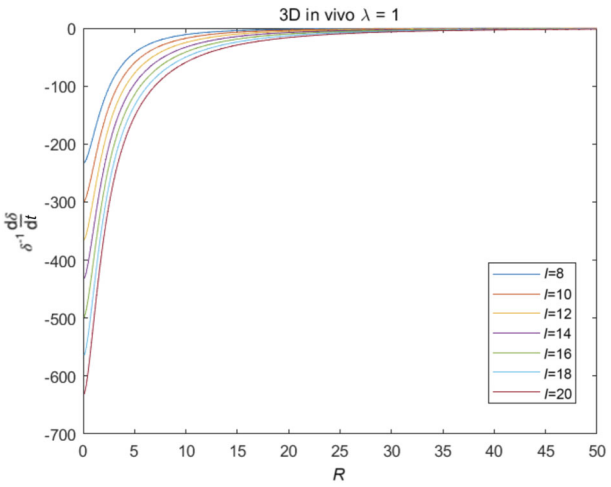

Fig. 12 3D in vivo, $G_0 = 1$, $c_B = 100$, $\lambda = 1.0$, $\ell = 8, 10, 12, 14, 16, 18, 20$, $R \in [0, 50]$

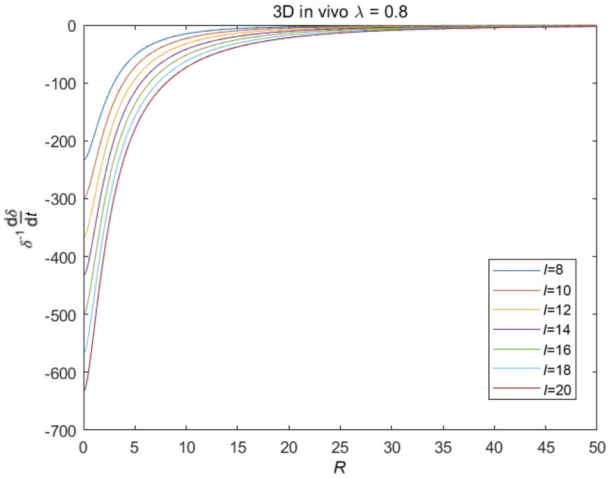

Fig. 13 3D in vivo, $G_0 = 1$, $c_B = 100$, $\lambda = 0.8$, $\ell = 8, 10, 12, 14, 16, 18, 20$, $R \in [0, 50]$

tumor boundary exceeds the threshold radius (R^*), namely, the tumor will evolve from an irregular shape to a circular shape before the threshold radius R^*. Then it will continue to evolve after R^*, but from a spherical shape to an irregular 3D shape.

ii. Fix a proper value of R_0, there exists ℓ_0 such that $M_2(\lambda, \ell, R) > 0$ for $\ell < \ell_0$ and $M_2(\lambda, \ell, R) < 0$ for $\ell > \ell_0$ (see Figs. 10, 11), which implies that when the tumor size is around R_0, the perturbation of the lower degree ℓ is easier to become unstable. However, the value of order m is canceled in (62), and thus the threshold of tumor radius is independent of the order m.

iii. With the size of the tumor expanding, $R(t)$ exceeds more threshold $R^*(\ell)$, therefore the corresponding degree ℓ perturbation becomes unstable successively.

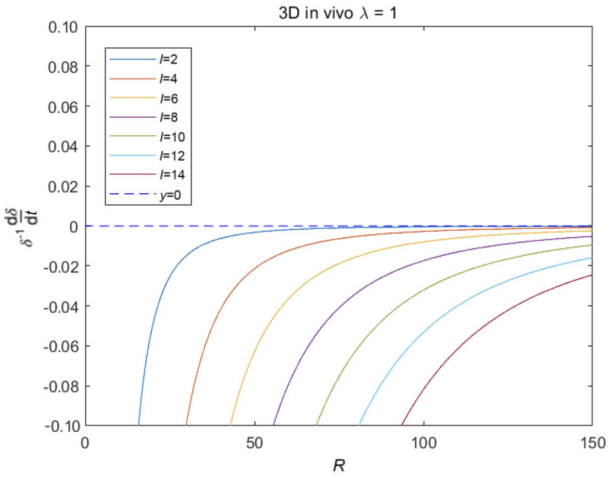

Fig. 14 3D in vivo $\lambda = 1$, $\ell = 2, 4, 6, 8, 10, 12, 14$, $R \in [0, 150]$

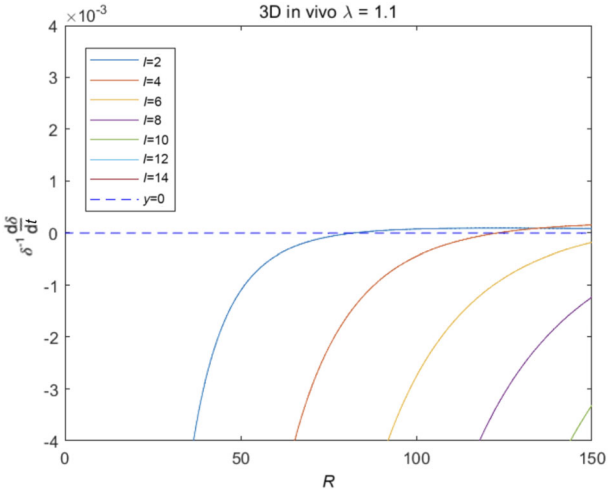

Fig. 15 3D in vivo $\lambda = 1.1$, $\ell = 2, 4, 6, 8, 10, 12, 14$, $R \in [0, 150]$

We hypothesize that there exists the threshold λ^* between 1.0 and 1.1, as shown in Figs. 14 and 15, since the evolution function remains negative when $\lambda = 1.0$ as in Fig. 14 and start going above $y = 0$ when $\lambda = 1.1$ as in Fig. 15.

Remark 6 Compared with the PME model (1), the incompressible limit model (5), (6) can also be seen as the sharp interface model. The rigorous analysis of such the incompressible limit is hard in general, and one can find [16–20, 26] as references. Unfortunately, due to the complicated nature of the analysis, currently, there is no direct evidence showing that we could find the relation between these two models in the sense of the boundary stability.

Corollary 1 *Fix $G_0 > 0$ and $C_B > 0$. For any $\lambda > 0$ and $\ell > 0$, $M_1(\lambda, \ell, R)$ for the in vitro model is given as*

$$\begin{cases} M_1(\lambda, \ell, R) \sim \dfrac{-10(\ell - 1)}{3} + O(R) \ \ as \ \ R \sim 0, \\ M_1(\lambda, \ell, R) \sim \dfrac{20\sqrt{\lambda}R}{(\ell + 1)\left(-\frac{1}{4}\ell^2 - \frac{1}{4}\ell + \frac{1}{2}\right)\ell} + O(1) \ \ as \ \ R \sim \infty. \end{cases} \tag{111}$$

Therefore, $M_1(\lambda, \ell, R) < 0$ as $R \to 0$ and as $R \to \infty$, thus $M_1(\lambda, \ell, R) < 0$ always holds, since $\ell \geqslant 1$ is always true. This indicates that the perturbation amplitude always decays for the in vitro model. Furthermore, for the in vivo model, we can infer from the figures that the function $M_2(\lambda, \ell, R)$ is always negative as $R \sim 0$, and is positive as $R \sim \infty$. The existence of the threshold can be shown by the intermediate value theorem, where the function $M_2(\lambda, \ell, R)$ must intersect the horizontal axis, changing the sign from negative to positive. This implies that the tumor boundary will change from stable to unstable. Note that the threshold $\lambda^*(\ell)$ may also depend on the degree ℓ as the perturbation parameter of spherical harmonics Y_ℓ^m. These can be seen more clearly in Figs. 10, 11, 12, 13. In order to determine the critical threshold value $\lambda^*(\ell)$, we expect to substitute the asymptotic expansions of modified Bessel functions and hyperbolic functions into the evolution function as in (105). The focus will be on the coefficient of the highest order term, as it dominates the behavior of $M_2(\lambda, \ell, R)$. By setting this leading coefficient to zero, we can ascertain the value of λ^* that induces a sign transition in $M_2(\lambda, \ell, R)$. This transition, from negative to positive in the evolution function, marks the critical point where the stability of the tumor changes.

5.2 2D and 3D Results Comparison

In our comparative analysis of 2D and 3D tumor growth models, as initially discussed in [10] and summarized in Sect. 2, we gained further insights into the tumor boundary stability in different dimensions. In summary, the 2D and 3D models are essentially the same, and they both exhibit similar divergences between the in vitro and in vivo models. Particularly, for both the in vitro 2D and 3D models, the evolution function consistently remains negative, indicating stable tumor boundaries.

For both the 2D and 3D in vitro models, the evolution function remains negative (indicating stability) when the consumption rate λ is below the threshold λ^*, where $\lambda^* = 1$ for the 2D model. Further investigation is required for the 3D model. When the rate exceeds this threshold, symbolized by λ^*, the function transitions from negative to positive, suggesting a shift from stable to unstable tumor boundaries. The threshold of the evolution function λ^* in the three dimensions, and its possible dependence on the wave number ℓ will be further studied and compared with the 2D scenario, beyond Figs. 14 and 15.

The stability of tumor boundaries is thus determined by the sign of the evolution function: a negative evolution function indicates stable boundaries, whereas a positive evolution function signals instability. This distinction is crucial for understanding the dynamic behavior of the tumor growth in different dimensional models, and the difference in 2D and 3D in vivo models marks the significance of our work.

6 Conclusion

In conclusion, this study leverages numerical methods to validate and extend the analytical results presented in [10] concerning 2D tumor PDE models and the boundary instability. By reconstructing and analyzing the main findings in [10], we successfully expanded these concepts into a 3D context. This extension is particularly significant as it offers a more applicable and insightful perspective on the tumor behavior, especially regarding its instability and potential malignancy. A key aspect of our approach is the combination of numerical simulations with analytical methods. This dual approach not only enriches our understanding of the tumor models but also serves as a cross-validation mechanism, ensuring the robustness of our findings.

During our research, we encountered two notable challenges in the numerical simulations, both of which provided significant insights. The first challenge arose when comparing the numerical tumor radius (R) over time against the analytical speed (σ) over time in [10]. The direct time derivative of numerical R data amplified errors, leading to impractical comparison results. We addressed this by integrating the analytical $\sigma - t$ data for direct comparison with the numerical $R(t)$ data, thereby minimizing error margins and aligning closely with analytical predictions in [10]. The second challenge involved the instability encountered in the ADI method when separately solving the reaction-diffusion equations for the tumor density u and the concentration c. Although the implementation of the ADI scheme was straightforward, its weakly decoupled system lacked the stability required for varied parameter inputs. To overcome this, we explored multiple splitting approaches within the ADI method, ultimately adopting the most stable splitting scheme.

In our final analysis, we examined the 3D in vivo evolution function by plotting it against various values of ℓ and λ. This led us to hypothesize the existence of a threshold, $\lambda^*(\ell)$, which may or may not be influenced by the order ℓ. We observed that the evolution function remains negative for $\lambda < \lambda^*(\ell)$, and transits from negative to positive as λ exceeds the threshold $\lambda^*(\ell)$. We propose that $\lambda^*(\ell)$ could be determined using a methodology akin to the asymptotic analysis presented in Corollary 1, and the boundary stability analysis in Sect. 5.3 in [10]. However, due to the limitations of numerical tools like Maple or Mathematica, currently, it is hard to find the explicit formation of $\lambda^*(\ell)$. We save such formation for future studies. Moreover, our intention encompasses extending beyond the current scope of the linear stability analysis, which primarily focuses on the perturbation $\cos(m\phi)$ in the two dimensions and $Y_\ell^m(\theta, \phi)$ in the three dimensions. Our planned trajectory involves incorporating nonlinear terms, aligning with our prospective research objectives.

Supplementary information Relevant code are available at: https://github.com/JiaqiZhang988/Tumor-Growth-PDE-Model-Relevant-Code

Appendix A 2D Numerics

A.1 Numerical Methods Introduction

To implement our numerical scheme in the 2D model, we describe the Ψ function for the in vivo regime as

$$\Psi(\rho, c) = \begin{cases} \lambda\rho c & \text{inside tumor } (\rho > 0), \\ -(c_B - c) & \text{outside tumor } (\rho = 0). \end{cases} \tag{A1}$$

Combining these, we define an $H(\rho)$ function to represent the function $\Psi(\rho, c)$ in numerical simulations, where

$$\Psi(\rho, c) = -(c_B - c) + (\lambda\rho c + (c_B - c))H(\rho), \tag{A2}$$

and we define the function $H(u)$ using the hyperbolic tangent function

$$\begin{cases} H(\rho) = \begin{cases} 0 & \text{if } \rho \leqslant 0, \\ \tanh(h\rho) & \text{if } \rho > 0, \end{cases} \\ H'(\rho) = \begin{cases} 0 & \text{if } \rho < 0, \\ k\text{sech}^2(h\rho) & \text{if } \rho > 0, \end{cases} \end{cases} \tag{A3}$$

where k is a constant, and the bigger the k is, the narrower the smooth part of the step function is. Including the hyperbolic function with the constant k gives us an approximation of the smoothed step function and helps us avoid the sharp change of the step function when using the indicator function $\mathbb{1}$, thus avoiding some problems brought by the steep step function in the numerical process.

A.1.1 2D ADI Model

The general PDEs for the 2D reaction-diffusion system based on (1) and (2), after rewriting the PME part (with power u^k), we have

$$\begin{cases} \rho_t = \dfrac{k}{k+1}((\rho^{k+1})_{xx} + (\rho^{k+1})_{yy}) + G_0 c\rho, \\ c_t = \dfrac{1}{\tau}(c_{xx} + c_{yy} - \Psi(\rho, c)). \end{cases} \tag{A4}$$

Therefore, using finite difference and rewriting the discrete points above as $\rho_{i+1,j}$, below $\rho_{i-1,j}$, to the right $\rho_{i,j+1}$ and to the left $\rho_{i,j-1}$ of the center point $\rho_{i,j}$, where i is the index in the x direction, and j is the index in the y direction, same applies to c.

We have the discretized version of this 2D reaction-diffusion system

$$\begin{cases} \dfrac{\rho_{i,j} - \rho_{i,j,\text{old}}}{\Delta t} = \dfrac{k}{k+1}\left(\left(\dfrac{\rho_{i,j+1}^{k+1} - 2\rho_{i,j}^{k+1} + \rho_{i,j-1}^{k+1}}{\Delta x^2}\right) + \left(\dfrac{\rho_{i+1,j}^{k+1} - 2\rho_{i,j}^{k+1} + \rho_{i-1,j}^{k+1}}{\Delta y^2}\right)\right) \\ \qquad\qquad + G_0 c_i \rho_i, \\ \dfrac{c_{i,j} - c_{i,j,\text{old}}}{\Delta t} = \dfrac{1}{\tau}\left(\left(\dfrac{c_{i,j+1} - 2c_{i,j} + c_{i,j-1}}{\Delta x^2}\right) + \left(\dfrac{c_{i+1,j} - 2c_{i,j} + c_{i-1,j}}{\Delta y^2}\right)\right) \\ \qquad\qquad - \dfrac{1}{\tau}\Psi(\rho_i, c_i), \end{cases} \tag{A5}$$

where ρ_c and $\rho_{c,\text{old}}$ represent the $u(x, y, t)$ values of the i, jth discretized grid points at the current time and the previous time, respectively. We then multiply both sides by Δt, move all terms to the same side, and use them as the functions where we apply Newton's method to find its zeros.

The IC for the density u takes the 2D axisymmetric form of the similarity solution of PME:

$$\rho(t = 0, r) = \left(1 - \frac{k}{4(k+1)^2}(r(t+1)^{\frac{-1}{2k+2}})^2\right)^{\frac{1}{k}}(t+1)^{\frac{-1}{k+1}}. \tag{A6}$$

The IC for the concentration c is the constant $c_B = 0.1$ in this 2D case. The BCs we used are still Neumann BCs at both ends of the x and y directions, that is

$$\begin{aligned} &\left.\frac{\partial \rho}{\partial x}\right|_{x=0} = 0, \quad \left.\frac{\partial c}{\partial x}\right|_{x=0} = 0, \quad \left.\frac{\partial \rho}{\partial x}\right|_{x=R} = 0, \quad \left.\frac{\partial c}{\partial x}\right|_{x=R} = 0, \\ &\left.\frac{\partial \rho}{\partial y}\right|_{y=0} = 0, \quad \left.\frac{\partial c}{\partial y}\right|_{y=0} = 0, \quad \left.\frac{\partial \rho}{\partial y}\right|_{y=R} = 0, \quad \left.\frac{\partial c}{\partial y}\right|_{y=R} = 0. \end{aligned}$$

The parameters remain the same as the 1D scenario, namely, the growth constant $G_0 = 1$, the consumption rate $\lambda = 0.5$ (involved in Ψ term), and the characteristic time scale of the nutrients evolution $\tau = 0.1$, and the constant for the approximated smoothed step function $k = 5$.

A.1.2 2D Axisymmetric Model

We also consider the 2D axisymmetric model for comparison. Since the Laplacian for 2D is

$$\Delta = \frac{1}{r}\frac{\partial \rho}{\partial r}\left(r\frac{\partial(\rho^{k+1})}{\partial r}\right), \tag{A7}$$

thus the general PDEs for the 2D axisymmetric model are

$$\begin{cases} \rho_t = \dfrac{k}{k+1}\dfrac{1}{r}\dfrac{\partial \rho}{\partial r}\left(r\dfrac{\partial(\rho^{k+1})}{\partial r}\right) + G_0 c\rho, \\ c_t = \dfrac{1}{\tau}\left(\dfrac{1}{r}\dfrac{\partial c}{\partial r}\left(r\dfrac{\partial(c)}{\partial r}\right) - \Psi(\rho, c)\right). \end{cases} \tag{A8}$$

Therefore, using the finite difference method and denote u at the center point as ρ_i with the discretization steps Δr and Δt, we have

$$\begin{cases} \dfrac{\rho_i - \rho_{i,\text{old}}}{\Delta t} = \dfrac{k}{k+1}\dfrac{1}{r_i \Delta r}\left[\dfrac{(r_i + 0.5\Delta r)(\rho_{i+1}^{k+1} - \rho_i^{k+1})}{\Delta r} - \dfrac{(r_i - 0.5\Delta r)(\rho_i^{k+1} - \rho_{i-1}^{k+1})}{\Delta r}\right] \\ \qquad\qquad + G_0 c_i \rho_i, \\ \dfrac{c_i - c_{i,\text{old}}}{\Delta t} = \dfrac{1}{\tau}\dfrac{1}{r_i \Delta r}\left[\dfrac{(r_i + 0.5\Delta r)(c_{i+1} - c_i)}{\Delta r} - \dfrac{(r_i - 0.5\Delta r)(c_i - c_{i-1})}{\Delta r}\right] - \dfrac{1}{\tau}\Psi(\rho_i, c_i), \end{cases} \tag{A9}$$

where ρ_i and $\rho_{i,\text{old}}$ represent the $u(x, t)$ values of the ith discretized grid point at the current time and the previous time, respectively. We then multiply both sides by Δt, move all terms to the same side, and use them as the functions where we apply Newton's method to find its zeros.

The IC for the density u and the concentration c is the same as the 2D ADI model, and the parameters are also the same. The BCs are the same, where we have Neumann BCs on both ends:

$$\begin{cases} \left.\dfrac{\partial \rho}{\partial r}\right|_{r=0} = 0, \quad \left.\dfrac{\partial c}{\partial r}\right|_{r=0} = 0, \\ \left.\dfrac{\partial \rho}{\partial r}\right|_{r=R} = 0, \quad \left.\dfrac{\partial c}{\partial r}\right|_{r=R} = 0. \end{cases} \tag{A10}$$

A.2 Numerical Methods Implementation

A.2.1 2D ADI for PME

In this section, we follow the ADI scheme introduced in [28] to solve the 2D PME and the reaction-diffusion equation systems in [10]. Specifically, we use the approximate factorization and numerically solve the 2D nonlinear PDE problem by solving the 1D nonlinear problem twice, namely, first in x, and then in the y direction.

We consider the PME in the two dimensions:

$$\rho_t = \nabla^2(\rho^{k+1}). \tag{A11}$$

Using the backward Euler implicit method in the finite difference method, we can discretize the equation

$$\frac{\rho - \rho^{\text{old}}}{\Delta t} = \nabla^2(\rho^{k+1}) + O(\Delta t). \tag{A12}$$

To use Newton's iteration method to solve this implicit scheme, we write

$$F(\rho) = \rho - \Delta t \nabla^2(\rho^{k+1}) - \rho^{\text{old}} + O(\Delta t^2). \tag{A13}$$

We set $\rho_0 = \rho^{\text{old}}$ and write $F(u) = 0$ as

$$\begin{cases} J_n \Delta\rho_n = -F_n, \\ \rho_{n+1} = \rho_n + \Delta\rho_n. \end{cases} \tag{A14}$$

Here, $J_n \Delta\rho_n = \frac{\delta F}{\delta \rho} \Delta u$ is the functional derivative of F (the Jacobian), which we approximate by $F(\rho + \Delta\rho) - F(u)$, plug in $\rho + \Delta\rho$ and ρ into (A13) and only keep the linear terms in $\Delta\rho$ and neglect the higher order terms, we can arrive at

$$\begin{aligned} J_n \Delta\rho_n &= F(\rho + \Delta\rho) - F(\rho) \\ &= \Delta\rho_n - \Delta t \nabla^2((k+1)\rho_n^k \Delta\rho_n) \\ &= \Delta\rho - \Delta t(k+1)(\rho_n^k \Delta\rho)_{xx} - \Delta t(k+1)(\rho_n^k \Delta\rho)_{yy}. \end{aligned} \tag{A15}$$

The matrix operators following this are (I: identity matrix)

$$(I - \Delta t D_{xx} - \Delta t D_{yy})\Delta\rho, \tag{A16}$$

where we denote $D_{xx} = (k+1)(\rho_n^k \Delta\rho)_{xx}$ and $D_{yy} = (k+1)(\rho_n^k \Delta\rho)_{yy}$.

Therefore, we can approximate the 2D Jacobian matrix J via

$$\begin{cases} (I - \Delta t D_{xx})(I - \Delta t D_{yy})\Delta u, \\ (I - \Delta t D_{xx} - \Delta t D_{yy} + O(\Delta t^2))\Delta u, \end{cases} \tag{A17}$$

where we can ignore the order $O(\Delta t^2)$ term, which means that we can use $(I - \Delta t D_{xx} - \Delta t D_{yy})$ as an approximation of $J_{n+1}\Delta u_{n+1}$, namely, $(I - \Delta t D_{xx} - \Delta t D_{yy}) \approx J \Delta u_{n+1}$.

Therefore, we have

$$(I - \Delta t D_{xx})[(I - \Delta t D_{yy})\Delta\rho] = -F_n, \tag{A18}$$

and let $v = (I - \Delta t D_{yy})\Delta\rho$, we have

$$\begin{cases} (I - \Delta t D_{xx})v = -F_n, \\ (I - \Delta t D_{yy})\Delta\rho = v. \end{cases} \tag{A19}$$

We first solve the D_{xx} equation to get v, and then substitute v into the D_{yy} equation to solve for $\Delta\rho$, which will be used to update the initial guess in the Newton iteration, and obtain improved approximation through each update until the solution converges.

Specifically, we first solve the D_{xx} equation for v (substitute in expression for D_{xx}:)

$$\begin{aligned}
&(I - \Delta t D_{xx})v = -F_n \\
&\Rightarrow v - \Delta t D_{xx} v = -F_n \\
&\Rightarrow v - \Delta t(k+1)(\rho^k v)_{xx} = -F_n \\
&\Rightarrow v_i - \Delta t(k+1)\left(\frac{\rho_{i+1}^k v_{i+1} - 2\rho_i^k v_i + \rho_{i-1}^k v_{i-1}}{\Delta x^2}\right) = -F_n.
\end{aligned} \tag{A20}$$

This can be expressed in the matrix form:

$$\left[I - (k+1)\frac{\Delta t}{\Delta x^2}\begin{pmatrix} -2\rho_i^k & \rho_{i-1}^k & & & \\ \rho_{i+1}^k & 2\rho_i^k & \rho_{i-1}^k & & \\ & \ddots & \ddots & \ddots & \\ & & \rho_{i+1}^k & 2\rho_i^k & \rho_{i-1}^k \\ & & & -2\rho_i^k & \rho_{i+1}^k \end{pmatrix}\right]\begin{pmatrix} v_1 \\ v_2 \\ \vdots \\ v_M \end{pmatrix} = \begin{pmatrix} F_1 \\ F_2 \\ \vdots \\ F_M \end{pmatrix}. \tag{A21}$$

Using backslash in MATLAB, we can get the vector v. Note that for this first step, we solve in the x direction, we take each row of the matrix F, and solve the corresponding vector v for each row of the matrix F. All vectors v together form a matrix v. Then we use a similar method to calculate Δu in the y direction. Note that we take each column of the matrix v, and use the matrix form $(I - \Delta t D_{yy})\Delta\rho = v$ to calculate corresponding $\Delta\rho$ for each column of v. Finally, we add $\Delta\rho$ on ρ_0 to update the initial guess and derive the numerical result of the solution ρ of PME using the 2D ADI scheme.

In summary, the key idea in the ADI scheme is to approximate the big Jacobian matrix (J) for the 2D PME by factorization in x and y directions, namely we factorize the Jacobian matrix $J = J_x J_y$, where $J_x = I - \Delta t D_{xx}$ and $J_y = I - \Delta t D_{yy}$.

A.2.2 2D Axisymmetric for PME

As introduced in the general 2D axisymmetric model, we have the finite difference discretization for the PME part, which is

$$\frac{k}{k+1}\frac{1}{r_i \Delta r}\left[\frac{(r_i + 0.5\Delta r)(\rho_{i+1}^{k+1} - \rho_i^{k+1})}{\Delta r} - \frac{(r_i - 0.5\Delta r)(\rho_i^{k+1} - \rho_{i-1}^{k+1})}{\Delta r}\right], \tag{A22}$$

where the IC is the similarity solution for the 2D axisymmetric version of PME as in (A6), and the BCs are the Neumann BCs at both ends, as given in (A10).

The parameters are $L = 20$, $T = 50$, $M = 100$, $N = 1\,000$, $k = 2$, where L is the total length, T is the final time, M is the number of grid points in spatial direction, N is the number of grid points in time discretization, and k is the power of the PME. We use Newton's method to obtain the approximated solution that we believe converges fast and well to the true solution. The check of this is achieved by drawing the plot of the similarity and numerical solutions in the same figure for comparison (Fig. A1). We also draw the log-log plot of the maximum of the approximated solution and the log-log plot of $(1+t)^{-1/4}$ in the same figure for comparison (Fig. A2).

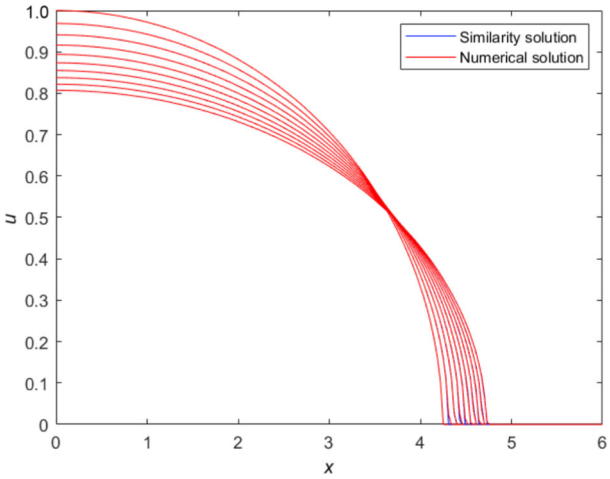

Fig. A1 2D axisymmetric PME-Comparison of numerical and analytical solutions

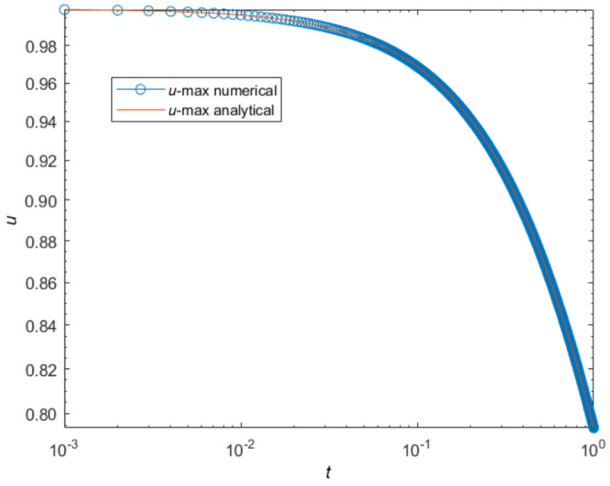

Fig. A2 Validation of 2D axisymmetric PME

A.2.3 2D ADI and 2D Axisymmetric Comparison

In this section, we consider the PME, and match up the 2D ADI method with the 2D axisymmetric case, thus proving that the ADI method is valid, and we can have an irregular shape or add perturbation (ϕ dependence) to be the IC and investigate the stability of the boundary after some time, namely simulating the perturbation analysis and the instability tumor boundary in the two dimensions and match up to [10]. Specifically, we try to compare with the 2D axisymmetric similarity solution starting from an IC in the center of a square ADI domain. Then we started with a different IC, like a small ellipse, and we saw that it became more and more circular.

A.2.4 Method for Matching up

First, we want to find the center of the initial shape, so that we can allow MATLAB to easily find the center of any irregular shape. This can be achieved by utilizing the mass conservation of PME with Neumann-Neumann BCs. Specifically, for $\rho_t = \nabla^2(\rho^k)$ with $\rho_x = 0$, we have

$$\int \rho \, \mathrm{d}A \ = \text{constant}, \quad \int x\rho \, \mathrm{d}A \ = \text{constant}, \quad \int y\rho \, \mathrm{d}A = \text{constant} \tag{A23}$$

and thus, the center $(\bar{x}, \bar{y})$ is

$$\bar{x} = \frac{\int x\rho \, \mathrm{d}A}{\int \rho \, \mathrm{d}A}, \quad \bar{y} = \frac{\int y\rho \, \mathrm{d}A}{\int \rho \, \mathrm{d}A}. \tag{A24}$$

In this way, we can do this calculation and get the position of the x and y center points calculated from the last time, so that we can define the center of any strange irregularly shaped tumor.

The top view of the result of ADI is the circular region. Thus, we can go from that center point and go to four radial directions of the circular region. Either one of these four directions can be used to check against the 2D axisymmetric case. Specifically, for the ADI, we use one of the directions and find its corresponding $\rho(r)$ with r going from the center to the endpoint, and draw the $\rho(r)$ versus r plot. We then compare this to the $\rho(r)$ versus r plot generated at the final time in the 2D axisymmetric case. We can see that the 2D ADI plot and the 2D axisymmetric case match up to be the same with the same IC.

This means that the 2D ADI can work to simulate the 2D axisymmetric tumor considered in [10]. The advantage of this is that for the axisymmetric case, we can not have any ϕ dependence and only depend on r, but for ADI, we can let the solution evolve in ϕ. This allows us to simulate the stability of the tumor boundary after some perturbation dependent on ϕ. Specifically, if we start from IC $\rho_0 = f(r)$, then for the tumor model, we will have some $\hat{\rho}_0 = f(r) + \epsilon g(\phi)$ (small perturbation depends on ϕ), which leads to a small change in the shape of the tumor. With the ADI code, we can observe the stability of the tumor, namely, does the tumor go back to being almost circular, or does the perturbation grow and the tumor shape changes from being nice to being more messy looking. Note that we also check that the ADI scheme by plotting the $U_{\max}$ versus time (t) and the $t^{-1/(k+1)}$ versus time (t) in the same log log plot and we can see that they fit together to be a straight line with a negative slope and are the same as each other. This is because the maximum of $\rho_{\max}(r) = t^{-1/(m+1)}$ and thus $\log(\rho_{\max}(r)) = (-1/(k+1)) \log t$.

The comparison is shown in Fig. A3, and we can see that the results from 2D ADI and 2D axisymmetric match up.

A.3 Validating Numerical Simulations Against Analytical Results and Predictions in [10]

A.3.1 2D ADI Reaction-Diffusion Systems Numerical Check for Analytical Results in [10]

We implement the 2D ADI scheme on the reaction-diffusion systems to numerically check against the analytical results in [10]. The discretization for the 2D axisymmetric reaction-diffusion system is given in (A5). For the BCs, we use the ghost point method to include the BCs in the F_u and F_c equations, where

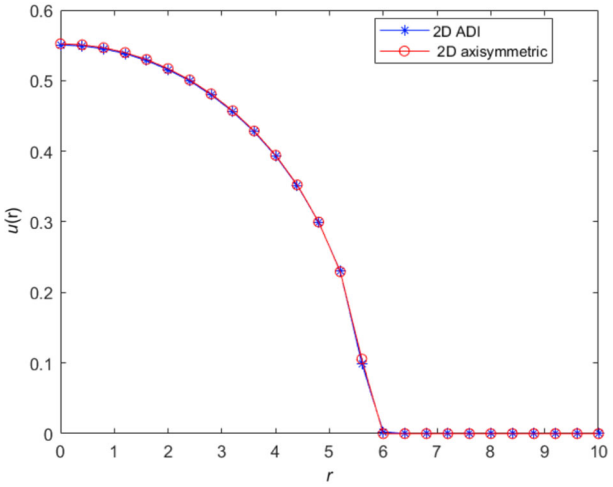

Fig. A3 Comparison of 2D ADI and axisymmetric

$$\begin{cases} F_{\rho_i} = \rho_c - \rho_{c,\text{old}} - \dfrac{k\Delta t}{k+1}\left(\left(\dfrac{\rho_p^{k+1} - 2\rho_c^{k+1} + \rho_k^{k+1}}{\Delta x^2}\right) + \left(\dfrac{\rho_u^{k+1} - 2\rho_c^{k+1} + \rho_d^{k+1}}{\Delta y^2}\right)\right) \\ \qquad - \Delta t G_0 c_i \rho_i, \\ F_{c_i} = c_c - c_{c,\text{old}} - \dfrac{\Delta t}{\tau}\left(\left(\dfrac{c_p - 2c_c + c_m}{\Delta x^2}\right) + \left(\dfrac{c_u - 2c_c + c_d}{\Delta y^2}\right)\right) + \dfrac{\Delta t}{\tau}\Psi(\rho_i, c_i). \end{cases} \tag{A25}$$

Then we use F_u, F_c to apply Newton's method as introduced before.

$\delta^{-1}\frac{d\delta}{dt}$ check for the in vivo model.

We also used the numerical simulation to check the perturbation analysis in [10]. The analytical results for the tumor boundary instability after perturbation are: for the in vivo model, when the consumption rate $0 < \lambda \leqslant 1$, if we fix any wave number $l \geqslant 2$ in the perturbation, then the instability will degenerate and the tumor boundary will become stable. Hence, the shape will change from irregular to circular with $0 < \lambda \leqslant 1$. On the other hand, if the consumption rate $\lambda > 1$, and we fix any wave number $l \geqslant 2$ in the perturbation, then there is a threshold radius R^*. This means that when the tumor radius $R \leqslant R^*$, then the tumor is stable, and after the radius exceeds R^*, the tumor will eventually become unstable. Therefore, the shape will change from irregular to circular and then become irregular again with $\lambda > 1$. The results showing the shape evolution of the tumor boundary are shown in Figs. 2, 3 in Sect. 2.

Acknowledgements This project is partially supported by the National Key R&D Program of China, Project Number 2021YFA1001200. J. Zhang is partially supported by the Summer Research Scholar program at Duke Kunshan University. X. Xu is partially supported by the National Science Foundation of China Youth Program, Project Number 12101278, and Kunshan Shuangchuang Talent Program, Project Number kssc202102066. The authors would also like to thank the helpful discussion with Yu Feng, Dang Xing Chen, and Lin Jiu.

Author Contributions This paper was completed by J. Zhang under the guidance and supervision of Prof. T. Witelski, Prof. J. Liu, and Prof. X. Xu. All authors contributed to refining the methodologies and to the writing and reviewing of the manuscript. Each author has read and approved the final version of the manuscript for publication.

Availability of Data and Materials Data and supporting materials for this work are available from the corresponding author upon reasonable request.

Code Availability Code of this work are available at https://github.com/JiaqiZhang988/Tumor-Growth-PDE-Model-Relevant-Code.

Declarations

Conflict of Interest On behalf of all authors, the corresponding author states that there is no conflict of interest.

References

1. Araujo, R.P., McElwain, D.S.: A history of the study of solid tumour growth: the contribution of mathematical modelling. Bull. Math. Biol. **66**(5), 1039–1091 (2004)
2. Baskaran, A., Lowengrub, J.S., Wang, C., Wise, S.M.: Convergence analysis of a second order convex splitting scheme for the modified phase field crystal equation. SIAM J. Numer. Anal. **51**(5), 2851–2873 (2013)
3. Bidan, C.M., Wang, F.M., Dunlop, J.W.: A three-dimensional model for tissue deposition on complex surfaces. Comput. Methods Biomech. Biomed. Eng. **16**(10), 1056–1070 (2013)
4. Browning, A.P., Maclaren, O.J., Buenzli, P.R., Lanaro, M., Allenby, M.C., Woodruff, M.A., Simpson, M.J.: Model-based data analysis of tissue growth in thin 3D printed scaffolds. J. Theor. Biol. **528**, 110852 (2021)
5. Byrne, H., Alarcon, T., Owen, M., Webb, S., Maini, P.: Modelling aspects of cancer dynamics: a review. Philos. Trans. R. Soc. A: Math. Phys. Eng. Sci. **364**(1843), 1563–1578 (2006)
6. Chen, W., Wang, C., Wang, X., Wise, S.M.: Positivity-preserving, energy stable numerical schemes for the Cahn-Hilliard equation with logarithmic potential. J. Comput. Phys. X **3**, 100031 (2019)
7. Cristini, V., Lowengrub, J., Nie, Q.: Nonlinear simulation of tumor growth. J. Math. Biol. **46**, 191–224 (2003)
8. Falcó, C., Cohen, D.J., Carrillo, J.A., Baker, R.E.: Quantifying tissue growth, shape and collision via continuum models and Bayesian inference. J. R. Soc. Interface **20**(204), 20230184 (2023)
9. Feng, Y., He, Q., Liu, J.-G., Zhou, Z.: Rigorous derivation of a Hele-Shaw type model and its non-symmetric traveling wave solution. arXiv:2404.16353 (2024)
10. Feng, Y., Tang, M., Xu, X., Zhou, Z.: Tumor boundary instability induced by nutrient consumption and supply. Z. Angew. Math. Phys. **74**(3), 107 (2023)
11. Friedman, A., Reitich, F.: Symmetry-breaking bifurcation of analytic solutions to free boundary problems: an application to a model of tumor growth. Trans. Am. Math. Soc. **353**(4), 1587–1634 (2001)
12. Greenspan, H.P.: Models for the growth of solid tumor as a problem by diffusion. Appl. Math. Comput. **30**, 215–222 (1972)
13. Gu, Y., Shen, J.: Bound preserving and energy dissipative schemes for porous medium equation. J. Comput. Phys. **410**, 109378 (2020)
14. Heinrich, M.A., Alert, R., LaChance, J.M., Zajdel, T.J., Košmrlj, A., Cohen, D.J.: Size-dependent patterns of cell proliferation and migration in freely-expanding epithelia. Elife **9**, 58945 (2020)
15. Heinrich, M.A., Alert, R., Wolf, A.E., Košmrlj, A., Cohen, D.J.: Self-assembly of tessellated tissue sheets by expansion and collision. Nat. Commun. **13**(1), 4026 (2022)
16. Jacobs, M., Kim, I., Tong, J.: Tumor growth with nutrients: regularity and stability. Commun. Am. Math. Soc. **3**(04), 166–208 (2023)
17. Kim, I., Požár, N.: Porous medium equation to Hele-Shaw flow with general initial density. Trans. Am. Math. Soc. **370**(2), 873–909 (2018)
18. Kim, I., Požár, N., Woodhouse, B.: Singular limit of the porous medium equation with a drift. Adv. Math. **349**, 682–732 (2019)
19. Kim, I.C., Perthame, B., Souganidis, P.E.: Free boundary problems for tumor growth: a viscosity solutions approach. Nonlinear Anal. **138**, 207–228 (2016)
20. Kim, I.C., Tong, J.: Interface dynamics in a two-phase tumor growth model. Interfaces Free Boundaries **23**(2), 191–304 (2021)
21. Liu, J.-G., Tang, M., Wang, L., Zhou, Z.: An accurate front capturing scheme for tumor growth models with a free boundary limit. J. Comput. Phys. **364**, 73–94 (2018)
22. Liu, J.-G., Wang, L., Zhou, Z.: Positivity-preserving and asymptotic preserving method for 2D Keller-Segal equations. Math. Comput. **87**(311), 1165–1189 (2018)

23. Lowengrub, J.S., Frieboes, H.B., Jin, F., Chuang, Y.-L., Li, X., Macklin, P., Wise, S.M., Cristini, V.: Nonlinear modelling of cancer: bridging the gap between cells and tumours. Nonlinearity **23**(1), 1 (2009)
24. Qian, Y., Wang, C., Zhou, S.: Convergence analysis on a structure-preserving numerical scheme for the Poisson-Nernst-Planck-Cahn-Hilliard system. CSIAM Trans. Appl. Math. **4**, 345–380 (2023)
25. Roose, T., Chapman, S.J., Maini, P.K.: Mathematical models of avascular tumor growth. SIAM Rev. **49**(2), 179–208 (2007)
26. Tong, J., Zhang, Y.P.: Convergence of free boundaries in the incompressible limit of tumor growth models. arXiv:2403.05804 (2024)
27. Vázquez, J.L.: The Porous Medium Equation: Mathematical Theory. Clarendon Press, Oxford (2006)
28. Witelski, T.P., Bowen, M.: ADI schemes for higher-order nonlinear diffusion equations. Appl. Numer. Math. **45**(2/3), 331–351 (2003)